PORTABLE WIRELESS ANTENNA SENSOR FOR SIMULTANEOUS SHEAR AND PRESSURE MONITORING

by

FARNAZ FARAHANIPAD

Presented to the Faculty of the Graduate School of

The University of Texas at Arlington in Partial Fulfillment

of the Requirements

for the Degree of

MASTER OF SCIENCE IN COMPUTER SCIENCE

THE UNIVERSITY OF TEXAS AT ARLINGTON

DECEMBER 2017

Acknowledgements

I would first like to express my sincere gratitude to my advisors Dr. Huang and Dr. Gao. I would like to appreciate Dr. Huang for her consistent and invaluable support and for her patience and immense knowledge. Without Dr. Gao's support, I was not able to finish this study. She supported me greatly and continuously.

It is my privilege to thank all my lab mates especially, Franck Tchafa and James Skilskyj and Jalal Fathi Sola for their help, cooperation and encouragement. You have my deep sense of gratitude for providing me such a great experience.

I would like to extend my thanks to Dr. Khalili and other faculty members at CSE department of UTA who offered collegial guidance and support over these two years.

Without any hesitation, I must appreciate and thank my parents who helped me grow as an independent and hard working woman who seeks to change the world. Of course, I need to give special thanks to my brother for all of his love and support.

Lastly and most of all, I would like to thank my devoted husband who has journeyed with me during my study. I owe an enormous debt of gratitude to him for his faith, encouragement and support.

November 20, 2017

Abstract

PORTABLE WIRELESS ANTENNA SENSOR FOR SIMULTANEOUS SHEAR AND PRESSURE MONITORING

Farnaz Farahanipad, MS

The University of Texas at Arlington, 2017

Supervising Professor: Haiying Huang and Jean Gao

Microstrip antenna-sensor has received considerable interests in recent years due to its simple configuration, compact size, and multi-modality sensitivity. Having a simple and conformal planar configuration, antenna-sensor can be easily attached on the structure surface for Structure Health Monitoring (SHM). As a promising sensor, the resonant frequency of the antenna-sensor is sensitive to different structure properties: such as planar stress, temperature, moisture, pressure and shear. As a passive antenna, antenna-sensor's resonant frequency can be wirelessly interrogated at a middle range distance without using an on-board battery. However, a major challenge of antenna-sensor's wireless interrogation is to isolate the antenna backscattering from the back-ground scattering to avoid "self-jamming" problem. To tackle this problem, we have developed an algorithm in order to eliminate back-ground structure backscattering.

This study develops antenna-sensor interrogation for simultaneous shear and pressure displacement sensing. A patch antenna was investigated as a shear and pressure sensing unit and an Ultra-Wide Band (UWB) antenna was added as a passive transceiver (Tx/Rx) for the antenna sensor. A microstrip delay line was implemented in sensor node to connect the Tx/Rx antenna and patch antenna-sensor. Due to time delay caused by the

delay line, the antenna backscattering can be separated from back-ground scattering in the time domain using time-gating technology. The gated time domain signal was converted into the frequency domain by Fast Fourier Transform (FFT), from which the resonant frequency of antenna-sensor can be determined.

Furthermore, we integrated the time-gating technique using the FMCW radar principle to realize FMCW time-gating interrogation technique to achieve a compact portable interrogation unit for wearable applications. The advantage of such an approach is that the time gating is performed in the frequency domain instead of the time domain. As a result, substantial improvement on the interrogation speed and the size of the interrogator can be achieved.

The proposed shear/pressure displacement sensor is intended to be used for monitoring the interaction between the human body and assistive medical devices (e.g. prosthetic liners, diabetic shoes, seat cushions) in order to enhance the comfort for the patients.

Table of Contents

List of Figures

List of Tables

Chapter 1

Introduction

1.1. Importance of shear and pressure sensor for structural health monitoring

Two types of forces exist at interface between two objects when they interact with each other: the force that is perpendicular to the interface is called the pressure force, while the force that is parallel to the interface is called the shear force. Measuring these two interfacial forces is crucial for many applications. For example, the human hand has the capability of perceiving the pressure as well as shear forces, which enable us to detect slippage and texture of objects[1]. Recently, there are increasing interest in developing tactile sensors for robots that can imitate the tactile sensation of human hands[2][3][4][5]. The combination of shear and pressure forces is also believed to play important roles in the ulceration of tissue, which has plagued the populations with diabetics[6][7], wheel chair users[8], amputees[9], and those who wear assistive medical devices. Embedding shear and pressure sensors in wearable devices such as diabetic shoes, seat cushions, prosthetic sockets, etc. will not only provide the needed guidance on how to adjust these devices for alleviating adverse conditions

but also could provide an important instrument for studying the etiology of pressure ulcers.

Different physical mechanisms have been exploited in the past to realize simultaneous shear and pressure sensors. Most of these sensors measure displacements, from which the response of the sensor to the shear and pressure forces are determined through calibration. Strain gauges were first used for shear and pressure measurements at the interface of a residual limb and a prosthetic socket[10]. Later, micro-machining technologies were introduced to reduce the sensor size and improve the spatial resolution, in which the strain gauges were replaced by other piezo-resistive sensing elements[11][12][13]. One drawback of the piezo-resistive sensors is that their resistance changes are typically very small and thus require delicate signal conditioning. The high power consumption of these sensors could also prevent them from being used in battery-powered portable monitoring systems. Shear and pressure sensing using capacitor arrays have been studied by several researchers[4],[14][15][16]. Additionally, they can be implements in flexible membranes and thus are more compatible with the human skins. But, capacitive sensors are sensitive to temperature and humidity. Inductive sensors have also been investigated to address the environmental sensitivity issues as well[17].

In order to measure shear and pressure displacement simultaneously, sensors usually become more complex and may require additional wiring for power. This large wire count severely limits the number of sensors that can be implemented in a distributed fashion. Multiple optical fiber sensors, on the other hand, can be implemented in one strand of optical fiber and thus have been studied for distributed shear and pressure sensing[18][19][20]. Unfortunately, the interrogation instruments for optical fiber sensors are usually bulky and expensive.

1.2. Patch antenna sensors

Another class of sensors that can enable distributed sensing is the electromagnetic (EM) resonant sensor[21][22][23][24][25][26]. Not only can these sensors be configured to sense multiple modalities simultaneously, they also can be interrogated using wireless means. Microwave patch antenna sensor is such an EM resonant sensor[27][28]. Antenna sensor technology has received high interest due to its low cost, compact size, passive operation and multi-modality sensitivity[27][29]. The most specific benefit of the antenna sensors is that it can be applied as wireless transceiver or passive sensor. Thus, these sensors can be implemented with minimum number of components.

1.3. Proposed sensor based on the microstrip patch antenna technology and its operation principle

A regular microstrip patch antenna usually consists of three components, namely a radiation patch, a di-electric substrate, and a ground plane, as shown in Figure 1. When a broad-band EM signal is supplied to the radiation patch through a microstrip transmission line, the signal whose frequency matches the antenna resonant frequency is radiated by the radiation patch while the remaining signal is reflected back. The spectrum of the reflected signal, therefore, displays significant losses at the antenna resonant frequencies.

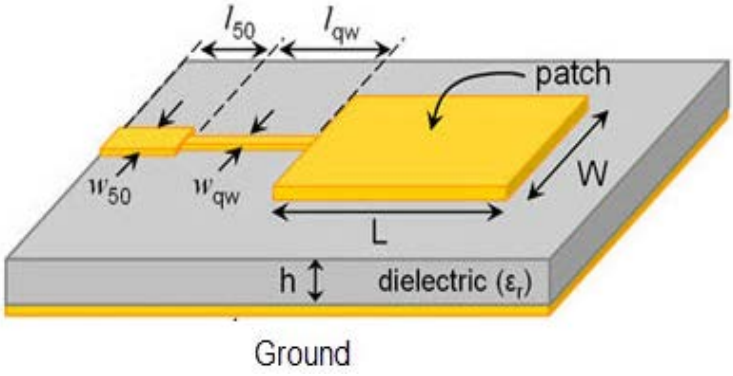

Figure 1-1 Microstrip rectangular patch antenna demonstration

To establish a shear pressure sensor, we can add a superstrate and a rectangular director above the radiation patch. A pressure and shear

forces applied to the sensor package deform the superstrate and cause changes in vertical or lateral position of the rectangular director. The resonant frequency of the patch will change due to the change in EM coupling between the radiation patch and director. Finally, by developing an algorithm, we are able to inversely determine the applied pressure and shear forces simultaneously.

1.4. Wireless interrogation of antenna sensor

A standard wireless sensing system can be separated into two parts: a wireless part to encode the sensing information into radio frequency (RF) and a wireless reader to decode the received RF signal and extract the original sensing information[30]. As a result, besides the benefit over the wired system, the setup is also improved.

In this work, an Ultra-Wide Band (UWB) antenna was added as a passive transceiver (Tx/Rx) for the antenna sensor. A wide broad-band signal is transmitted towards the antenna sensor through UWB (Tx/Rx). A microstrip delay line was added to the sensor node between Tx/Rx antenna and sensor. It is assumed that we can extract the resonant frequency of the antenna sensor by analyzing the reflected signal from the sensor node and calculate the applied shear and pressure due to the changes in frequencies.

The problem is that the backscattering signal from sensor node consists of both the antenna backscattering and back-ground clutter, which creates "self-jamming" problem[27].

1.5. Objectives in this research

In order to use wireless interrogation, a major challenge is to tackle the self-jamming problem. In the other word, the antenna backscattering should be isolated from back-ground clutter. In this thesis, we have developed a program in order to isolate the antenna backscattering from the received wireless signal by time-gating. Also in order to inversely determine shear and pressure displacement, simultaneous shear and pressure experiment on antenna-sensor was performed.

The scientific merits of this proposed research are:

1) Develop time gating technique, based on either software or hardware, to eliminate self-jamming problem;

2) Implement and characterize antenna sensor for simultaneous shear and pressure sensing;

3) Established a method to characterize di-electric for any material using microstrip patch antenna;

4) Develop UWB antennas on flexible substrate;

5) Higher sensitivities for shear and pressure displacement are achieved.

Chapter 2

Microstrip patch antenna

2.1. Principle of micro strip Antenna operation

A microstrip rectangular patch antenna consists of three components, namely a radiation element, a di-electric substrate, and a ground plane, as shown in Figure 2-1 (a). Functioning as an electromagnetic (EM) resonator, a regular microstrip patch antenna radiates EM signals at its resonant frequencies. When a broadband EM signal is supplied to the radiation patch through a microstrip transmission line, the signal whose frequency matches the antenna resonant frequency is radiated by the radiation patch while the remaining signal is reflected back. The spectrum of the reflected signal, therefore, displays significant losses at the antenna resonant frequencies. This phenomenon is represented by a S_{11} curve that plots the return loss of the patch antenna as a function of the incident frequency, as shown in Figure 2-1 (b).

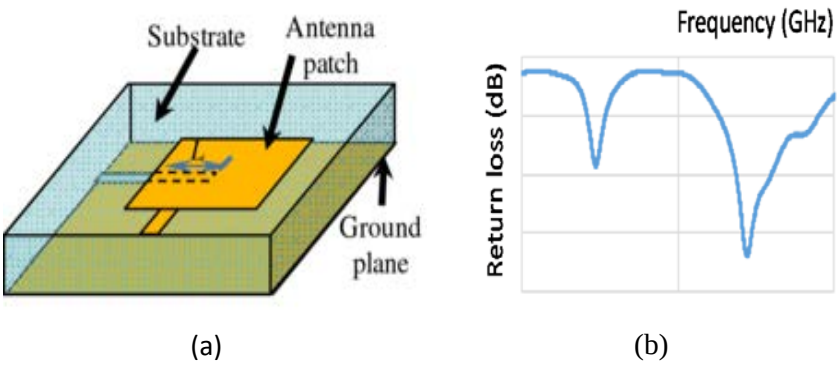

Figure 2-1 (a) microstrip patch antenna consisting of a ground plane, a rectangular radiation element, and a di-electric substrate; (b) typical S_{11} curve of a microstrip patch antenna.

2.2. Patch antenna as shear and pressure sensor

The simultaneous shear and pressure sensor is essentially a stacked microstrip patch antenna consisting of a regular patch antenna, a superstrate, and a director, as shown in Figure 2-2.

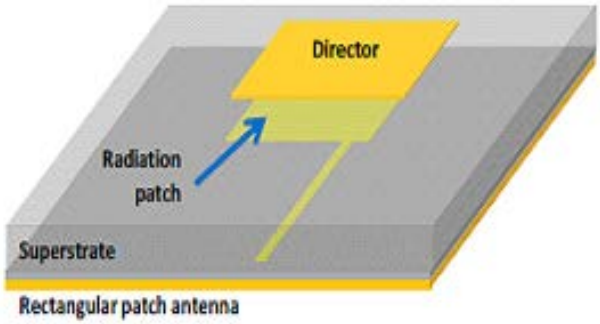

Figure 2-2 A shear/pressure displacement sensor consists of a microstrip patch antenna and a director that is separated from the radiation patch by a superstrate;

The resonant frequencies of a regular microstrip patch antenna are determined by the dimensions of the radiation patch as well as the di-electric properties of the substrate material. A microstrip patch antenna with a rectangular radiation patch, for example, has two fundamental resonances. The resonance with the lowest frequency, i.e. the TM_{01} resonance, corresponds to the length of the radiation patch, while the resonance at the second lowest frequency, i.e. the TM_{10} mode, corresponds to its width. Based on the transmission line model[31], the resonant frequencies of a microstrip patch antenna are determined by the dimensions of the radiation patch and its effective di-electric constant ε_{re} as:

$$f_{mn} = \frac{c}{2\pi\sqrt{\varepsilon_{re}}} \sqrt{\left(\frac{m\pi}{L}\right)^2 + \left(\frac{n\pi}{W}\right)^2} \quad , \qquad (1)$$

here c is the speed of light in vacuum, L is the length of the antenna patch, and W is the width of the antenna patch. f_{10} and f_{01} represent the resonant frequencies of the TM_{10} and TM_{01} resonances, respectively.

From various analytical models for microstrip patch antenna, the transmission line model is chosen for this study due to its simplicity. Studying the electric field propagation of microstrip line shows that part of the electric field lines travels in-to air instead of the di-electric substrate (Figure 2-3).

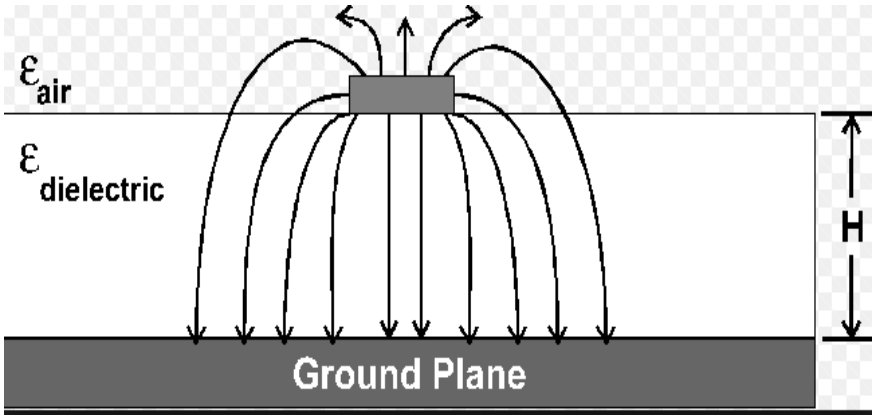

Figure 2-3 Electric field lines in transmission line model; Radiation from Microstrip antenna can occur from the fringing fields between periphery of patch and ground-plane

Hence, by considering fringing and wave propagation, an effective di-electric constant ε_{reff} is introduced. For a microstrip patch antenna having air as its superstrate (i.e. the un-loaded antenna), its effective di-electric constant is approximately equal to the di-electric constant of the substrate. When a superstrate and a metallic director are placed on top of the radiation patch, the effective di-electric constant of the antenna is contributed by the di-electric constant of the superstrate as well[32].

In addition, the antenna resonant frequencies are also sensitive to the vertical and lateral positions of the director due to the EM coupling between the radiation patch and the director. As an instance, by applying the pressure depicted in Figure 2-4 (a), the distance between the radiation patch and the director is decreased which in turn shifts the antenna

resonant frequencies. The shear forces also change the lateral position of the director (in the x-direction) as shown in Figure 2-4 (b), which again results in shifting the antenna resonant frequencies. Measuring the two antenna resonant frequencies, therefore, enables deducing the shear and pressure displacements of the director simultaneously.

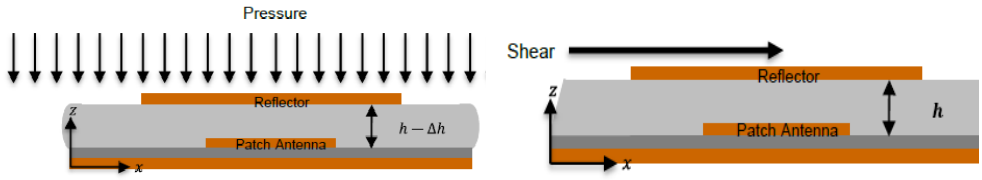

(a) (b)

Figure 2-4 Effects of pressure and shear forces on microstrip patch antenna ;(a) Vertical displacement between patch antenna and reflector due to compression;(b) Lateral displacement between patch antenna and reflector due to shear deformation.

There is no need to explain that, to accurately define the resonant frequency of the microstrip patch antenna, di-electric constant of superstrate should be determined. In the next chapter, the steps to define the effective di-electric constant and design process of antenna are explained.

Chapter 3

Shear and pressure antenna sensor

3.1. Sensor design and fabrication

Various software tools can perform electromagnetic analysis of different kinds of antenna. Here, we used Sonnet Pro 16.52 due to its user-friendly graphical interface and its accuracy for regular shapes of patches. The steps for initial design of microstrip patch antenna with superstrate are provided in this chapter.

The configuration of the antenna shear and pressure displacement sensor as well as its design parameters are shown in Figure 3-1. A rectangular director was selected due to its simplicity. The director was chosen to be wider than the radiation patch so that a slight shift of the director along the width direction of the radiation patch does not have any effect on the antenna resonant frequencies (see Figure 3-1 (a)) .On the other hand, the director only covers a portion of the radiation patch along its length direction. The length direction of the radiation patch is therefore the shear direction of the antenna sensor.

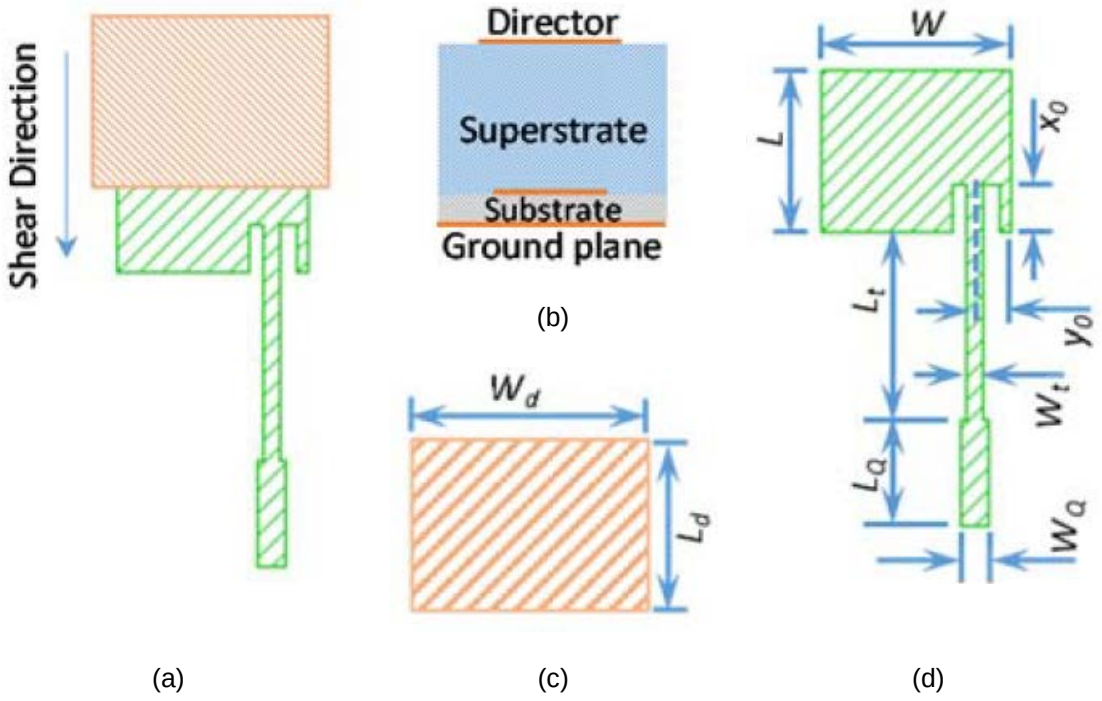

Figure 3-1 Configuration and design parameters of the antenna shear/pressure displacement sensor: (a) top view; (b) side view; the radiation patch is embedded between the substrate and superstrate; (c) director dimensions; (d) radiation patch and microstrip transmission line dimensions.

The side view of the antenna sensor is shown in Figure 3-1 (b). The components with a solid golden fill (i.e. the ground plane, the radiation patch, and the director) are conductive while the components with a hatched fill (i.e. the substrate and superstrate) are di-electric materials. The design parameters include the di-electric constant ε_{re1} and thickness h_1 of the substrate, the length *L* and width *W* of the radiation patch, the di-electric

constant ε_{re2} and height h_2 of the superstrate, as well as the shape, dimensions, and position of the director placed on top of the superstrate. In addition, the radiation patch will be fed by a microstrip transmission line terminated with a 50 Ω subminiature version A (SMA) connector to excite the resonance modes. In order to achieve impedance matching among the radiation patch, the microstrip transmission line, and the SMA connector, inset feeding and a quarter-wavelength (Q-λ) impedance transformer have to be designed. The design parameters for the feeding mechanism include the inset feeding location (x_0,y_0), the length L_t and width W_t of the microstrip transmission line, and the length L_Q and width W_Q of the Q-λ transformer. A commercial high frequency di-electric laminate with a di-electric constant of 3.48 and a thickness of 1.52 mm (RO4350B from Rogers Corp.) was selected as the substrate material. Silicone rubber, which is commonly used in commercial prosthetic liners, was selected as the superstrate material. The height of the superstrate was selected to be 5 mm, which is the typical thickness of prosthetic liners. Since silicone rubber can vary widely in compositions. The di-electric constant of silicone rubber has to be characterized experimentally.

3.2. Simulate the effects of superstrate on the antenna resonant frequencies

We need to know the effective di-electric constant of superstrate in order to select the length and width of the patch properly. To evaluate the effects of the superstrate on the antenna resonant frequencies, a single-frequency patch antenna with a 5 mm thick superstrate was designed and modeled using an EM simulation tool (Sonnet Pro 16.52). The simulated S_{11} curves of the antenna indicates that the antenna resonant frequency shifts to lower values as the superstrate di-electric constant increases, as depicted in Figure 3-2.

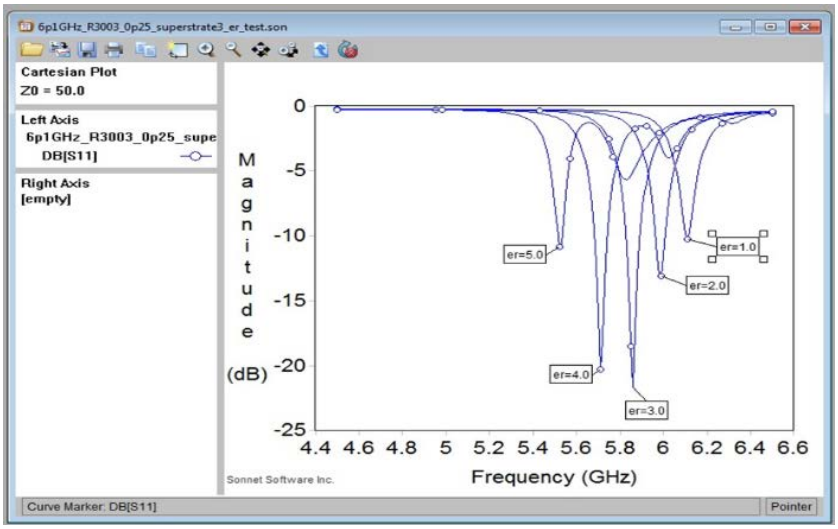

Figure 3-2 The simulated S_{11} curves of the antenna with different superstrate di-electric constant.

Based on the resonant frequency shifts, we can inversely determine the effective di-electric constant of the superstrate-loaded antenna from the f_{res} frequency[32], i.e.,

$$\mathrm{f_{res}} = \frac{\mathrm{c}}{2\mathrm{L}\sqrt{\varepsilon_{\mathrm{re}}}} \,. \qquad (2)$$

The effective di-electric constants, ε_{re} , calculated using Equation 2 and the simulated antenna resonant frequencies, are summarized in Table 1 and plotted in Figure 3-3. The effective di-electric constant, calculated from the simulated antenna resonant was 3.676 for the un-loaded antenna and it increases linearly with the superstrate di-electric constant.

Table 1 Relationship between the superstrate di-electric constant and the effective di-electric constant of the superstrate-loaded antenna

Di-electric Constant	Resonant Frequency (GHz)	Effective Di-electric Constant
1	6.11	3.0315
2	5.99	3.154
3	5.86	3.295
4	5.71	3.471
5	5.52	3.714

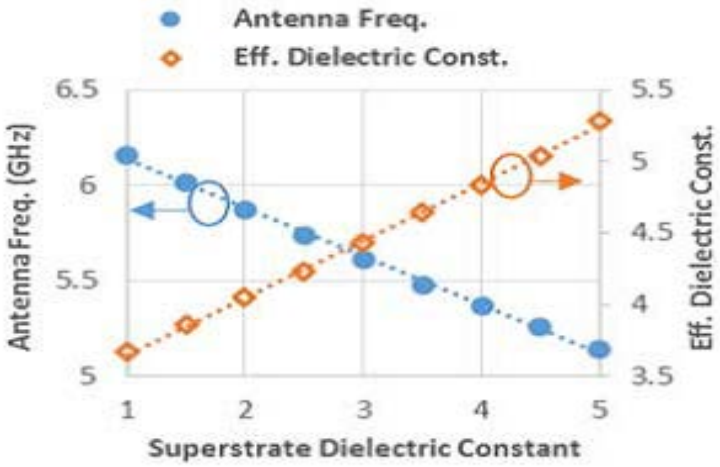

Figure 3-3 Effect of superstrate di-electric constant on the antenna resonant frequency of a single –frequency patch antenna and the effective di-electric constant derived from the simulated antenna resonant frequency shift.

The single-frequency patch antenna was fabricated from a substrate with double sided copper clad using a chemical etching technique. The frequency of the fabricated patch antenna was measured with and without the superstrate. Due to the variability associated with the fabrication process, the fabricated antenna without the superstrate had a resonant frequency of 5.96 GHz, while the simulated resonant frequency was 6.16 GHz. The difference between the simulated and measured frequencies is around 3%. Placing the superstrate on top of the radiation patch shifted the antenna resonant frequency to 5.78 GHz. Due to the discrepancy between the simulated and measured antenna frequencies, the measured frequency

cannot be used directly for obtaining the superstrate di-electric constant from Figure 3-3. To compensate for the discrepancy, the effective di-electric constant of the silicone-loaded antenna was calculated using equation (6) in [32], the measured antenna frequencies of the loaded and unloaded antenna (f_r = 5.78 GHz, f_{r0} = 5.96 GHz) and the effective di-electric constant of the unloaded antenna (ε_{r0}= 3.676), which resulted in an effective di-electric constant of 3.9 for the superstrate-loaded antenna. Based on Figure 3-3, the di-electric constant of the silicone superstrate was then determined to be 1.63, which is much smaller than the values of between 3.0 to 4.0 reported in [33] [34]. We obtained similar di-electric constant values for a 2 mm thick superstrate and the 5 mm thick superstrate using a patch antenna with a much thinner substrate. In both cases, the simulation model was modified to reflect the thickness changes. Therefore, the smaller di-electric constant obtained is likely due to the composition of the prosthetic liner material, which is much softer than the silicone materials that are used for antenna Radomes.

This approach can be used in the future to experimentally determine the di-electric constant of any superstrate material and incorporate the measured di-electric constant in the antenna sensor design process. As such, a more realistic antenna design model can be established for sensor optimization and parametric study.

3.3. Sensor design and simulation

Based on the measured superstrate di-electric constant and based on the literature review[35], the sensor size was chosen to be around 10 mm. Following the antenna design procedure described in [35], the f_{01} and f_{10} frequencies were selected to be 6 and 7 GHz, respectively, which resulted in a radiation patch of 12.1 mm in width and 10.2 mm in length. The width of the microstrip transmission line was chosen to be 1.0 mm, which has an impedance of 90 Ω for an effective di-electric constant of 3.9. The inset feeding location (x_0, y_0) was calculated accordingly using the approach described in[35]. Finally, the impedance of the Q-λ transformer was calculated as 67 Ω, where Z_{50} represents the 50 Ω impedance of the SMA connector and Z_t = 90 Ω is the impedance of microstrip transmission line. The corresponding width and length of the Q- λ transformer are 1.9 mm and 6.7 mm, respectively. The width of the director was chosen to be 16 mm, which leaves a 2 mm margin on each side of the radiation patch along the width direction. As such, the antenna sensor is not sensitive to slight lateral movements of the director.

The length of the director controls the sensitivities and overall size of the sensor, which in turn determines its spatial resolution; a shorter director results in lower sensitivities but a finer spatial resolution while a longer

director leads to high sensitivities and coarser spatial resolution. As a trade-off, the length of the director was chosen to be 12 mm. The sensor design was modelled in Sonnet Pro. A three dimensional (3D) view of the simulation model is shown in Figure 3-4. The simulation box was 100 mm wide and 150 mm long with a cell size of 0.05 mm square, resulting in 2000X3000 cells in total. The top surface of the simulation box was assigned to be free space while the other five surfaces were assumed to be lossless metal. The space between the director and the top surface had a height of 10 mm and was filled with air.

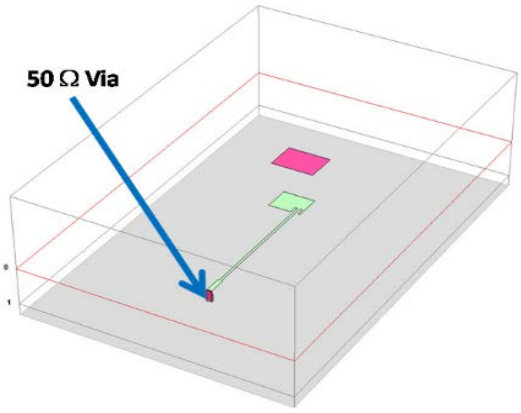

Figure 3-4 Three-dimensional view of the antenna shear/pressure displacement sensor simulated using an electromagnetic simulation tool (Sonnet Pro 16.52).

To excite the patch antenna, a square via with a dimension of 1 mm by 0.2 mm and a 50 Ω port were placed at the end of the microstrip transmission line. To reduce the computational time, the analysis was

carried out using “adaptive sweep”. Due to the inset feeding, the impedances of the two antenna resonances are coupled.

Table 2 Design parameters of antenna shear and pressure displacement sensor

ε_{r1}	substrate di-electric constant	3.48
h_1	substrate thickness	1.52 mm
ε_{r2}	superstrate di-electric constant	1.63
h_2	superstrate thickness	5.0 mm
ε_{re}	effective di-electric constant	3.90
L	radiation patch length	10.2 mm
W	transmission line length	12.1 mm
L_t	transmission line width	50 mm
W_t	transmission line width	1 mm
L_Q	Q-□transformer length	6.7 mm
W_Q	Q-□transformer width	1.9 mm
L_d	director length	12 mm
W_d	director width	16 mm
(x_0, y_0)	transmission line feeding position	(2.2,3.0)mm

To find an optimized feeding location, a parameter sweep on (x_0, y_0) was carried out when the director covered one half of the radiation patch along its length direction and was centered along the width direction of the radiation patch (see Figure 3-1 (a)). The finalized design parameters of the antenna sensor are given in Table 2.

3.4 Optimize the antenna sensor design to achieve sufficient sensitivities

The effects of the director position on the antenna resonant frequencies were studied by assuming that the neutral position of the director, i.e. with zero pressure and shear displacements, is when the director is 5 mm above the radiation patch and its lower edge is aligned with the center line of the radiation patch. The superstrate height was varied from 5 mm to 3.6 mm at an interval of 0.2 mm, resulting in a total pressure displacement of 1.4 mm. At each pressure displacement, the director was shifted along the shear direction from s = -4 mm to 4 mm at an increment of 1 mm, where s = -4 mm corresponds to when the lower edge of the director is 4 mm above the center of the radiation patch. The effects of the shear and pressure displacements on the antenna resonant frequencies are shown in Figure 3-5.Both frequencies increased with the increase of the pressure displacement, i.e. as the director was moved closer to the radiation

patch. Similarly, under a constant pressure displacement, the antenna frequencies increased as the director was moved toward the transmission line.

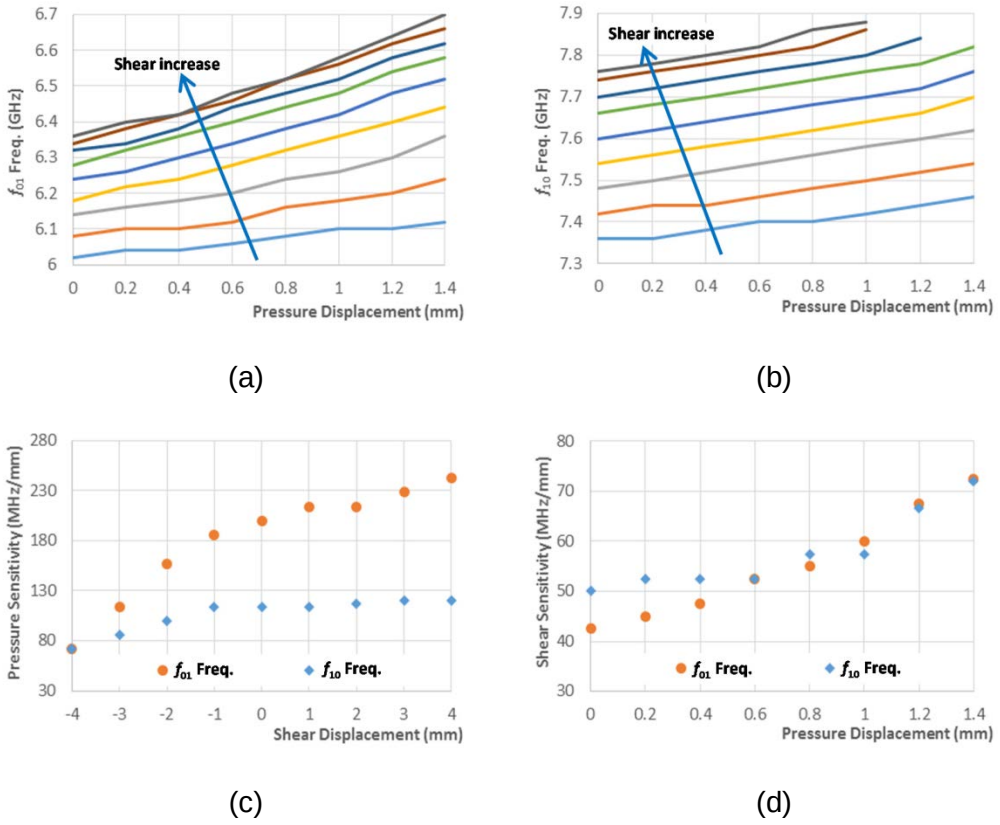

Figure 3-5 Simulated results - effects of the shear and pressure displacements on the (a) f_{01} and (b) f_{10} antenna frequencies and their (c) shear and (d) pressure sensitivities

At large shear displacements, i.e. when the director was very close to the feeding location, both frequencies become less sensitive to the shear displacement, as shown in Figure 3-5(a) and Figure 3-5(b). In addition, the TM_{10} resonance weakened significantly and it was difficult to detect the f_{10}

frequency when both the shear displacement and the pressure displacement are large, resulting in missing data points for pressure displacements larger than 1.0 mm (see Figure 3-5 (b)). The average shear and pressure sensitivities were calculated at different pressure and shear displacements, respectively. As shown in Figure 3-5(c), the shear sensitivities are similar for the two antenna resonant frequencies, ranging from around 40 MHz/mm at zero pressure to slightly above 70 MHz/mm when the pressure displacement was 1.4 mm. The pressure sensitives of the antenna resonant frequencies are about two to three times larger than the shear sensitivities. For both frequencies, the pressure sensitivities increased linearly with the shear displacement increase when the shear displacement was negative. These sensitivity increases, however, leveled off when the shear displacement became positive. In addition, the f_{01} frequency displayed much higher pressure sensitivity than the f_{10} frequency did.

3.5 Sensor fabrication and characterizing

The dual-frequency microstrip patch antenna was fabricated following the same fabrication procedure described above while the director was cut from a thin flexible laminate (Rogers RO3003, 0.125 mm thick). The three components of the antenna shear and pressure displacement sensor,

i.e. the rectangular patch antenna, the superstrate, and the director are shown in Figure 3-6. The patch antenna and the director were taped on base plates using Kapton tape so that they can be installed on a test apparatus that can apply controlled shear and pressure displacements automatically.

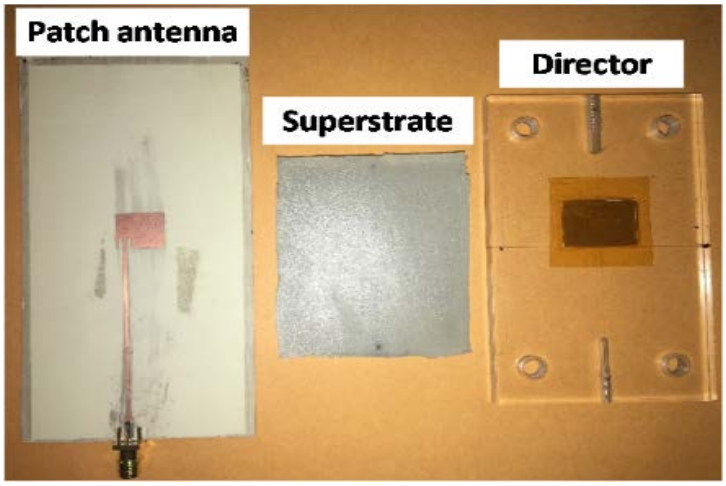

Figure 3-6 Components for the antenna shear/pressure displacement sensor.

The superstrate was cut from a commercial prosthetic liner and glued on the patch antenna using an instant-bonding ethyl adhesive (Loctite 4011). The antenna resonant frequencies before and after the application of the adhesive were almost identical, indicating that the adhesive has little effect on the antenna resonant frequencies. The measured S_{11} curves of the antenna sensor without the superstrate, with the superstrate, and with the director placed at the neutral position are compared with their simulation counterparts in Figure 3-7. Again, due to the fabrication variability, the

measured frequencies of the antenna sensor without the superstrate were slightly smaller than the simulated values. As predicted by the simulation model, the measured antenna frequencies shift to lower frequencies when the superstrate was placed on top of the radiation patch.

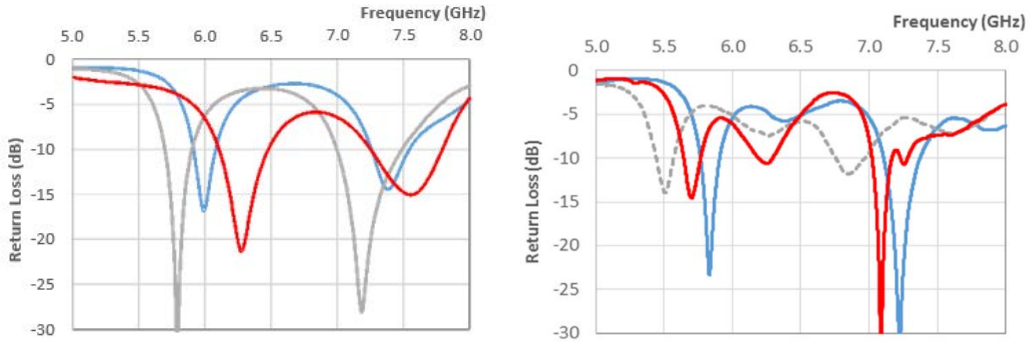

(a) (b)

Figure 3-7 Effects of the superstrate and director on the resonant frequencies of the dual-frequency patch antenna; (a) simulation and (b) measurement.

Similarly, adding the director shifted the antenna frequencies higher. However, the frequency increases due to the director were much smaller than those predicted by the simulation. While the measurement results matched with the simulation model qualitatively, it is, in general, difficult to achieve an exact match between the simulation and measurement due to the sensitivity of the antenna sensor to minute fabrication variations and the difficulty in modeling the nuances of the experiments. For example, the

simulation model has a perfect 50 Ω port while soldering may change the impedance of the SMA connector in the experiment. Moreover, the superstrate covers the entire design space, including the port, in the simulation model. In contrast, the superstrate only covers a portion of the microstrip transmission line in the experiment. Other factors, such as the thickness of the superstrate, which was difficult to measure precisely using a caliper due to the softness of the material, and the alignment of the director may also contribute to the observed discrepancies. Therefore, the simulation is only used for the initial design of the antenna sensor but the performance of the antenna sensor was characterized and validated experimentally.

3.6. Shear and pressure test set up

A test apparatus that enables applying controlled shear and pressure displacements to the antenna sensor package was implemented and is shown in Figure 3-8. The base plate containing the director was installed on the top plate, which is fixed along the vertical direction but can freely slide along the horizontal direction. The base plate containing the patch antenna and the superstrate was installed on the bottom plate that is mounted above a bubble actuator and can freely slide along the vertical direction. Inflating the bubble actuator pushes the bottom plate upward, generating a pressure

force on the sensor package. The displacement of the bottom plate was measured using a linear variable differential transformer (LVDT) distance sensor. To apply shear displacements, a rod was screwed on the top plate so that its position can be adjusted using a linear motor.

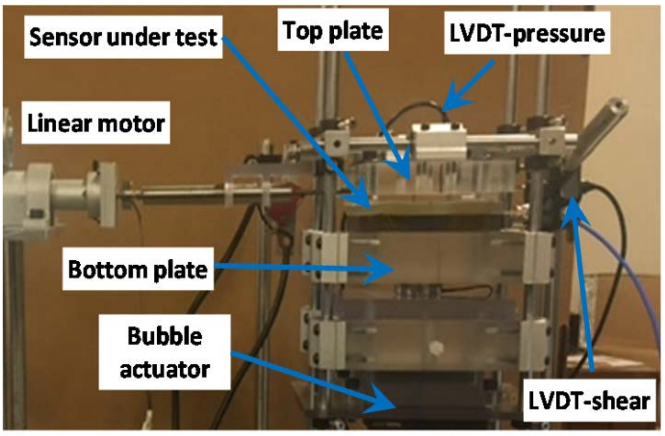

Figure 3-8 Mechanical test apparatus for applying controlled shear and pressure displacements on the antenna sensor under test

Shear displacement of the top plate was also measured using an LVDT distance sensor, mounted on the opposite side of the shear rod. The resonant frequencies of the microstrip patch antenna were measured by connecting it to a vector network analyzer (VNA) (Rohde & Schwarz, ZVA24) using a coaxial cable. The VNA was set to sweep the interrogation frequency from 5 GHz to 8 GHz with 5001 frequency points, resulting in a frequency resolution of 0.6 MHz. An Arduino-based controller was implemented to control the applied shear and pressure displacements and to acquire the shear and pressure displacements from the LVDT sensors.

A visual-basic program was developed in Microsoft Excel to communicate with the controller and to acquire the S_{11} parameters from the VNA automatically. The shear and pressure test was first carried out without gluing the director to the superstrate so that the shear displacement range can be evaluated. Based on this initial test, the neutral position of the director was determined. Subsequently, the director was glued to the superstrate using the same adhesive that glued the superstrate to the radiation patch. After the adhesive was cured, the director was moved away from the neutral position so that the antenna sensor can be tested under different combinations of shear and pressure displacements.

3.7. Results of shear and pressure testing of the antenna

The shifts of the antenna resonant frequencies with the applied shear and pressure displacements are plotted in Figure 3-9 (a) and (b). The total pressure displacement applied was 0.78 mm, corresponding to pressurizing the bubble actuator from 0 kPa to 273 kPa at an interval of 19.5 kPa. The total shear displacement was 5.94 mm, i.e. the director was moved from -4.08 mm to 1.86 mm at 13 increments. Both antenna frequencies reduced initially when the pressure displacement was increased from 0 mm to 0.15 mm. Subsequently, the antenna frequencies increased linearly with the

increase of the pressure displacement. The inconsistency of the antenna frequency shifts at the low pressure displacements, which is not predicted by the simulation, may be contributed by a thin layer of fabric laminated on the outer surface of the commercial prosthetic liner.

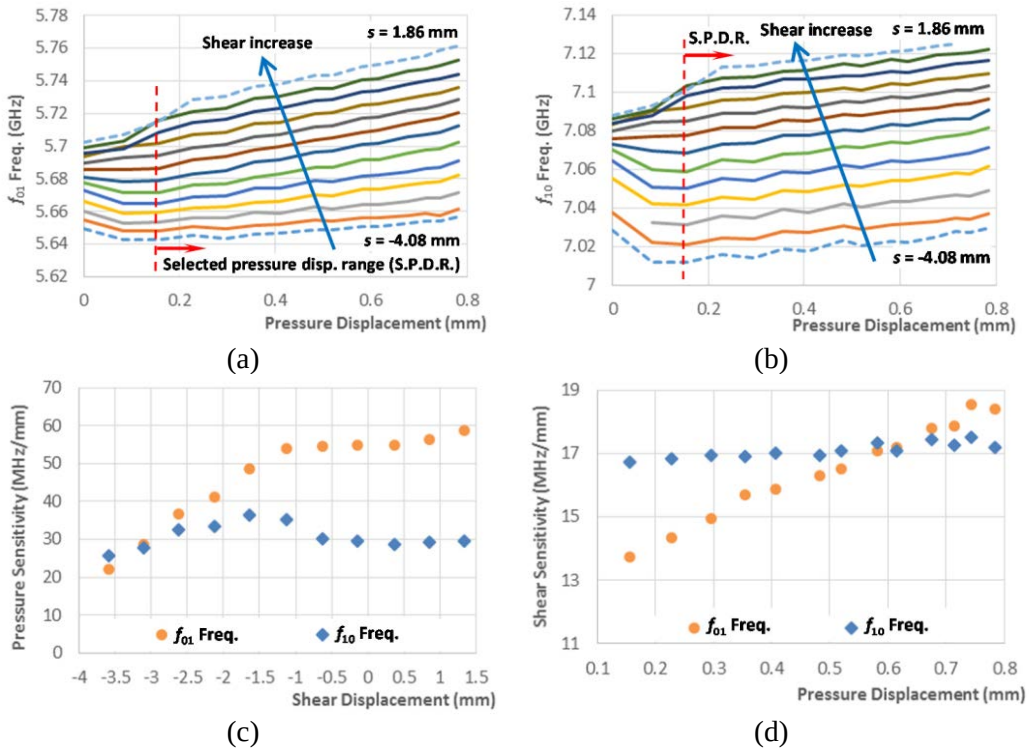

Figure 3-9 Measurement results - effects of shear and pressure displacements on the (a) f_{01} and (b) f_{10} antenna frequencies and their (c) shear and (d) pressure sensitivities for the selected operation range of pressure displacements from 0.15 mm to 0.78 mm and shear displacements from -3.6 mm to 1.35 mm. In (a) and (b), only the solid curves, *i.e.* the curves obtained within the shear displacement operation range, were selected for the inverse algorithm.

Considering that the thin fabric is relatively porous, its thickness and di-electric constant may experience large changes at the initial application of pressure. These parameters, however, will stabilize once the pressure reaches a threshold, beyond which the antenna frequencies are mainly influenced by the compression of the silicone rubber. Another contributor may be the alignment of the bottom plate, which cannot be perfectly leveled initially. We observed that the bottom plate tended to self-level under slight pressure. Since the antenna sensor is unlikely to operate at near zero pressure condition, the measurements obtained below 0.15 mm pressure displacements were excluded, resulting in a pressure operation range of 0.15 mm to 0.78 mm.

As a result, the shear operation range of the antenna sensor is defined as from -3.6 mm to 1.35 mm. The shear and pressure sensitivities of the antenna resonant frequencies for the selected operation range are shown in Figure 3-9 (c) and (d). The shear sensitivity of the f_{01} frequency varies almost linearly from 13 MHz/mm to 19 MHz/mm as the pressure displacement increases while the shear sensitivity of the f_{01} frequency remains almost constant at around 17 MHz/mm. The pressure sensitivities of both frequencies increase steadily when the shear displacement was increased from -3.6 mm to -1.6 mm. The shear sensitivities, however, leveled off when the shear displacement was increased beyond -1.1 mm.

Qualitatively, the trends of the measured antenna frequency shifts as well as the shear and pressure sensitivities matched with the simulation predictions. However, the measured sensitivities were three or four times smaller than the simulated values. Again, these discrepancies are likely due to the fact that the simulation model cannot faithfully capture the details of the experiment setup. For example, the simulation model only accounted for the position changes of the director but did not consider the di-electric constant change of the silicone rubber under shear or pressure deformations.

3.8. Results and discussion

In order to inversely determine the shear and pressure displacements from the measured antenna resonant frequencies, a MATLAB program was developed to curve fit the measurement data using bi-variable quadratic functions, $f_{ij}=P_{00}+P_{10}.s+P_{01}.p+P_{11}.s.p+P_{20}.s^2+P_{02}.p^2$ where s is the shear displacement, p is the pressure displacement, and f_{ij} stands for either f_{01} or f_{10}. R^2 values of 0.9978 and 0.9990 were achieved for the f_{01} and f_{10} frequencies, respectively. The 3D views of the fitting surfaces as well as the measured data are shown in Figure 3-10 (a) and (b). Based on these fitting equations, an algorithm was developed to extract

the shear and pressure displacements from measured antenna resonance frequencies.

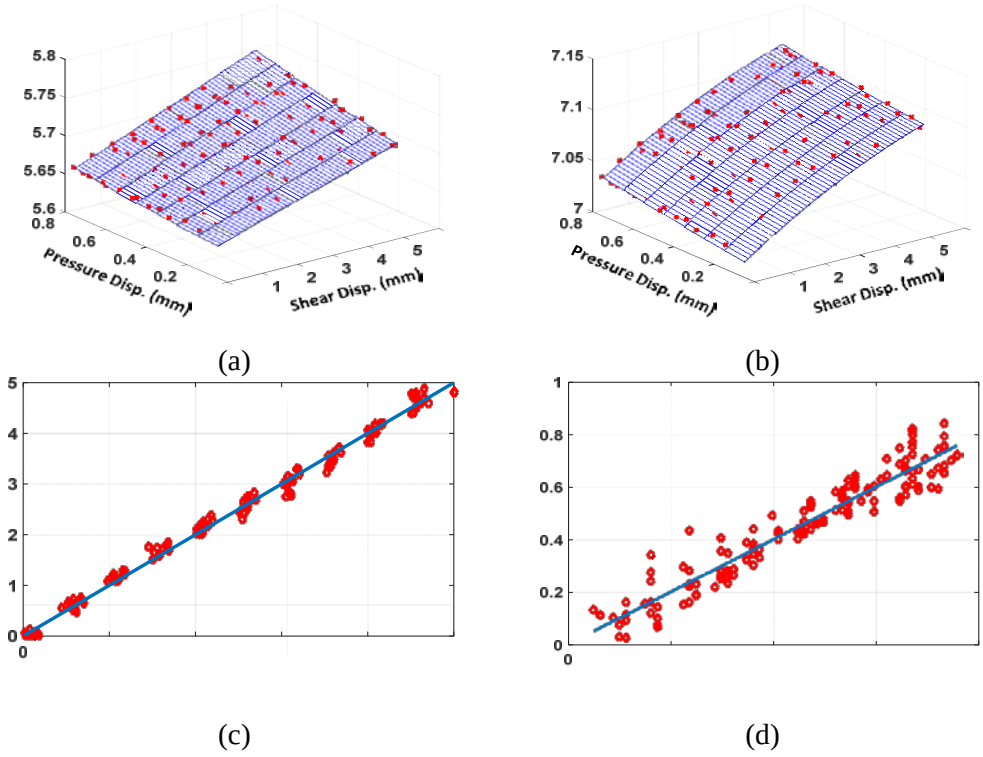

Figure 3-10 Deduce the shear and pressure displacements from the measured antenna resonant frequencies; (a) and (b) curve fitting the measured f_{01} and f_{10} frequencies as a bi-variable quadratic function; (c)and (d) comparisons between the shear and pressure displacements inversely determined from the measured f_{01} and f_{10} frequencies with the actual inputs. The blue line represents a perfect match between the estimated and actual values.

The inverse algorithm searches the entire shear operation range s with an increment of 0.01 mm. For each assumed *s* value, the pressure displacement *p* is solved from the f_{01} fitting equation, which is a single-

variable quadratic function once s and f_{01} are known. The resulting (s, p) pairs are subsequently plugged into the f_{10} fitting equation to calculate the estimated f_{10} frequency. The difference between the estimated and measured f_{10} frequencies was then recorded. After the entire shear displacement range was searched, the (s, p) value that gives the lowest difference between the estimated and measured f_{10} frequencies was selected as the measured shear and pressure displacements.

The measured shear and pressure displacements, i.e. the values inversely determined from the antenna resonant frequencies, are compared with their actual inputs in Figure 3-10(c) and (d). Except a few outliers, the errors between the measured displacements and the actual inputs are typically within 0.3 mm for the shear displacements and within 0.15 mm for the pressure displacements, corresponding to 5% of the full shear displacement range and 25% of the full pressure displacement range, respectively.

Some of the measurement errors may be contributed by the LVDT sensors, which have measurement uncertainties of 0.06 mm. The measurement errors for the shear displacements are comparable to those of the published sensors [6], while the measurement errors for the pressure displacements, in terms of the percentage of the full range, is slightly higher than that of the pressure sensor commercialized by Tekscan[36], which is

widely used in clinical applications. It is worth noting that we were not able to apply pressures beyond 273 kPa to the bubble actuator due to the equipment limitation. Therefore, the full pressure displacement range of the antenna sensor may be larger than what we have obtained in this study. Reducing the height of the superstrate in the future may improve the range and measurement uncertainties of the antenna sensor, especially for the pressure measurements. In addition, we also noticed that the test apparatus introduced slight coupling between the shear and pressure displacements due to the bubble actuator. Replacing the bubble actuator with a linear motor may improve the measurement uncertainties as well.

In this study, the antenna sensor was characterized with respect to the shear and pressure displacements. The corresponding shear and pressure forces or stresses can be calculated from the measured displacements once the mechanical properties, namely the shear and compression moduli, of the superstrate material are known. Considering that the shear and pressure stresses for different applications vary widely [6][36], the mechanical properties of the superstrate material should be characterized and adjusted for specific applications.

Chapter 4

Wireless interrogation of embedded antenna sensor

4.1. Introduction of UWBs and its principle of operation

Wireless sensors have many advantages over traditional wired sensors. Sensor installation and maintenance costs are much lower for wireless sensors because the need for cables is eliminated. In addition, the mobile nature of wireless sensors also makes reconfiguration of the sensor networks easier. Using wireless communication as the sensor interrogation method eliminates the physical limitation on the maximum number of sensors that can be interfaced to a monitoring system.

Antennas began to be used as an electrical part in wireless communication in 1888, Heinrich Hertz (1857-1894) were first demonstrate the existence of radio waves[37]. The UWB antennas became popular for wireless interrogation due to its wide frequency range for communication.

Figure 4-1 Rectangular monopole Ultra-Wide Band antenna; Back and front side

The ideal antennas for UWB system have proper broad operating bandwidth for impedance matching and high gain radiation for different directions. There are various kinds of UWB models but the monopole planer antenna type is the most common one, which is shown in Figure 4-1. The monopole planer has wide bandwidth, simple structure, easy fabrication and it is inexpensive. It has been demonstrated that rectangular UWB antennas with the partial ground are able to support multiple resonant modes compare to one with complete ground plane[38]. These closely overlapped resonant modes, as shown in Figure 4-2, can achieve a wide bandwidth.

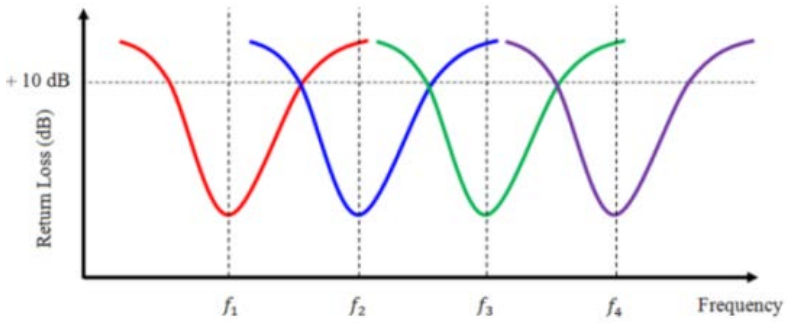

Figure 4-2 Closely overlapped resonance mode for monopole antennas

In this chapter, the design and implementation of a compact microstrip Ultra-Wide Band (UWB) antenna are explained. Due to complex calculation and difficulties in fabrication process, we propose a method to

design the UWB antenna using the transmission line model that we used for antenna sensor design. The fabricated UWB has the capability of operating between 3.4 GHz to 8.6 GHz.

4.2. UWB design and implementation

The UWB Tx/Rx microstrip antenna was designed with a 0.25 mm thick RO3003 as the flexible substrate: The design started with a conventional patch antenna having a perfect ground plane. The resonant frequency of the conventional microstrip antenna f was chosen to be at 6.11 GHz which resulted in a radiation patch that is 14.1 mm in length and 17.3 mm in width. A transmission line width of 0.6 mm was chosen. To increase the bandwidth of the antenna, the ground plane has to be reduced to partially cover the radiation patch, as shown in Figure 4-3 (a). Simulations of the antenna with perfect ground and partial ground were carried out, followed by the parametric study on the height of the ground plane and the width of the microstrip feed line. The optimum result for partial ground is shown in Figure 4-3 (b).

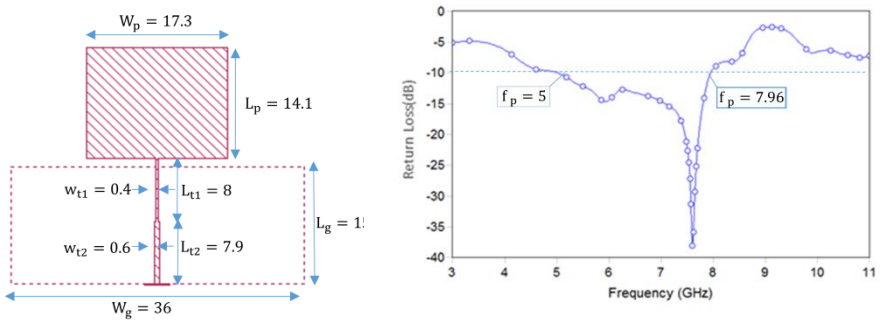

(a) (b)

Figure 4-3 The design of the UWB Tx/Rx antenna; (a) numerical simulation model developed in Sonnet Pro 16.52; (b) simulated S_{11} parameter of the UWB Tx/Rx antenna. The -10 dB bandwidth is determined to be from 5 GHz to 7.96 GHz.

The final design parameters of the UWB Tx/Rx microstrip are given in Table 3.

Table 3 Design parameter of UWB Tx/Rx microstrip antenna

εr1	substrate di-electric constant	3.0
h1	substrate thickness	0.25 mm
L	radiation patch length	14.1 mm
w	radiation patch width	17.3 mm
Lt	transmission line length	8 mm
Wt	transmission line width	0.4 mm
Lt2	quarter transmission line	7.9 mm
Wt2	quarter transmission line width	0.6 mm
Lg	ground patch length	15 mm
Wg	width of the feed microstrip line	0.6 mm

The UWB Tx/Rx microstrip antenna was fabricated on commercial substrate (RO3003 from Rogers Crop.) with a di-electric constant of 3 and

a thickness of 0.25 mm. The front and back views of the UWB antenna fabricated using chemical etching are shown in Figure 4-4 (a).

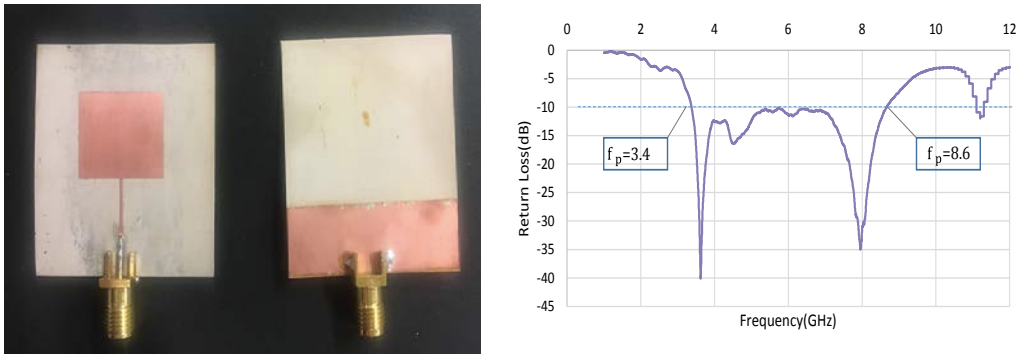

(a) (b)

Figure 4-4 Fabricated UWB Tx/Rx microstrip antenna and its S_{11} parameter measured using a Vector Network Analyzer (VNA); (a) Front and back view of the fabricated UWB Tx/Rx microstrip antenna; (b) the measured S_{11} curve. The -10 dB bandwidth of the UWB Tx/Rx antenna is from 3.4 GHz to 8.6 GHz.

The measured S_{11} curve is plotted in Figure 4-4 (b) validates that the UWB Tx/Rx antenna fabricated on a 0.25 mm flexible substrate has sufficient band-width. The gain of the Tx/Rx antenna, measured using a two-port transmission test, is shown in Figure 4-5. The antenna shows a relatively flat gain between 6 and 8 dBi in frequencies ranging from 5.75 to 7 GHz.

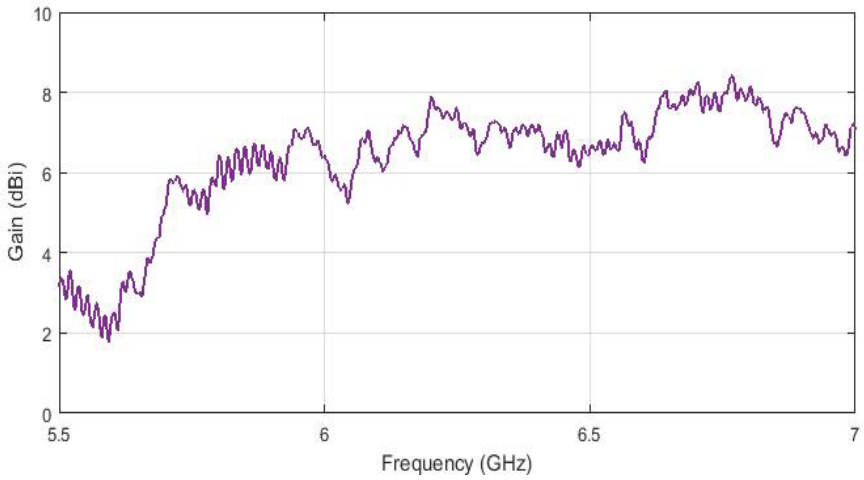

Figure 4-5 Measured radiation gain of the fabricated Tx/Rx antenna

4.3. Wireless interrogation based on antenna backscattering

A major challenge of antenna sensor's wireless interrogation is to isolate the antenna backscattering from the back-ground scattering to avoid "self-jamming" problem. This can be achieved by connecting the antenna sensor to a UWB Tx/Rx antenna using a transmission line, as shown in Figure 4-6. The UWB Tx/Rx antenna receives the wide band signal transmitted from the interrogator and resends the reflected signal from the sensor node to wireless interrogator with a time delay. As a result, the antenna backscattering can be distinguished from back-ground scattering due to the round trip transmission on the delay line in time domain.

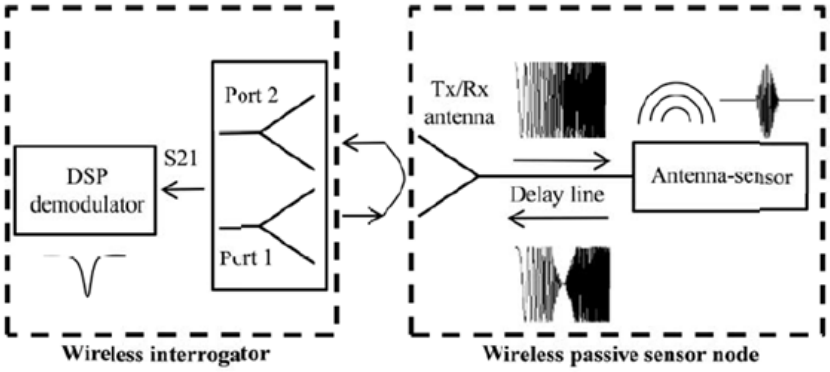

Figure 4-6 Block diagram of wireless sensing system of a wireless passive antenna sensor.

4.4. Design the sensor package and characterizing transmission line length

To generate a delay between the received and the reflected signals in the sensor side, we can use a long transmission line between Tx/Rx antenna and the antenna-sensor. The time delay *(t)* caused by the transmission line can be calculated from the length of transmission line *x*, the substrate di-electric constant ε_r , and the speed of light *c* as:

$$t = x\sqrt{\varepsilon_r}/c \quad . \tag{3}$$

Table 4 shows the calculated time delay caused by different lengths of a transmission line fabricated on substrate (RO3003) based on Equation 3.

Table 4 Calculated time delay caused by different transmission line length

Length of Transmission line (mm)	**Calculated Delay (ns)**
100	1.15
150	1.86
200	2.35
250	2.94

The delay times are also simulated with the Sonnet pro software for transmission line with lengths of 100,150, 200 and 250 mm and the results are shown in Figure 4-7. The simulated results and calculated values agreed with each other very well.

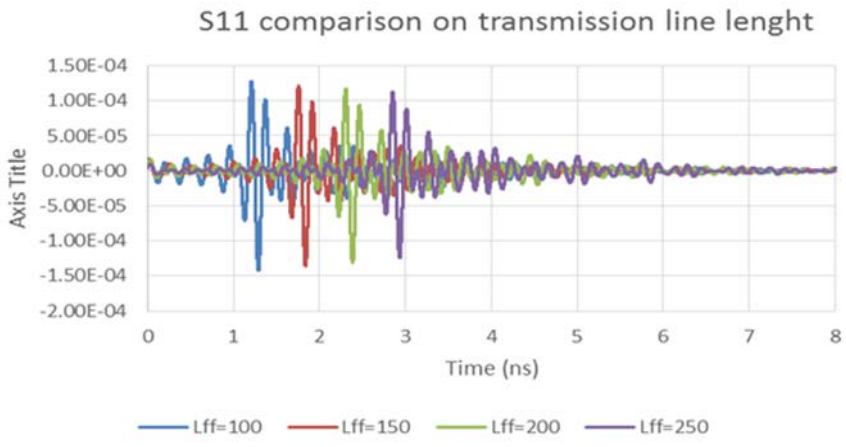

Figure 4-7 Simulated time delays with different transmission line lengths

4.5. Sensor design and fabrication

By considering the transmission line model for simulation, as explained in previous chapters, the f_{01} and f_{10} frequencies were selected to be 5.35 and 6 GHz, respectively, which resulted in a radiation patch that is 13.5 mm in length and 14 mm in width. For the design of the microstrip transmission line, a typical transmission line with length of 100 mm, 150 mm and 200 mm and width of 0.62 mm was chosen, the sensor design was modelled in Sonnet Pro. Due to the inset feeding, the impedances of the two antenna modes are coupled. To find an optimized feeding location, a parameter sweeps on (x_0, y_0) was carried out. The design parameters of double frequency patch antenna are shown in Table 5. The fabricated sensors are shown in Figure 4-8.

Table 5 Design parameters of antenna shear and pressure sensor

ε_{r1}	substrate di-electric constant	3.0
h_1	substrate thickness	0.25 mm
L	radiation patch length	13.5 mm
W	radiation patch width	14 mm
L_t	transmission line length	100,150,200 mm
W_t	transmission line width	0.6 mm
(x_0, y_0)	transmission line feeding position	(3.0, 3.0) mm

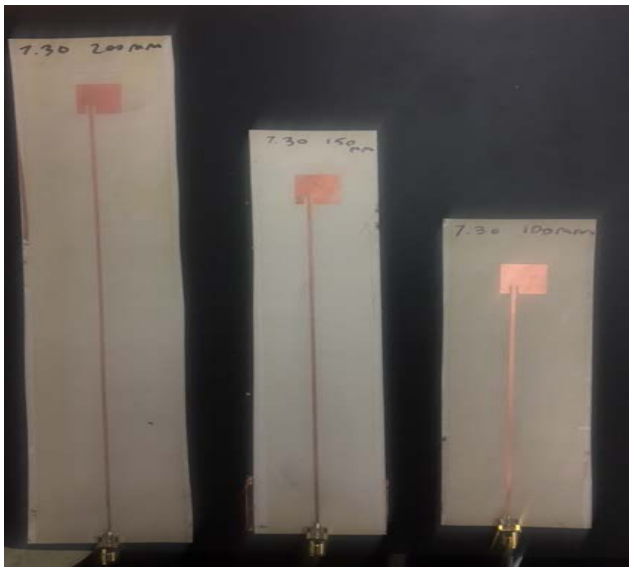

Figure 4-8 Fabricated sensor with different transmission line lengths

4.6. Validating time delay by experiment

We developed a MATLAB program to extract the time delay caused by the transmission line. The S_{11} parameter which is in the frequency domain is converted to the time domain, which clearly shows when the sensor signal arrives. We applied the same processing on all three sensors to validate the result. As a result, the simulation results demonstrated reasonable agreement with the measurement results. Figure 4-9, displays the time delay for simulated and fabricated sensors with different transmission line length.

Simulated results | Measured results

L=100 mm

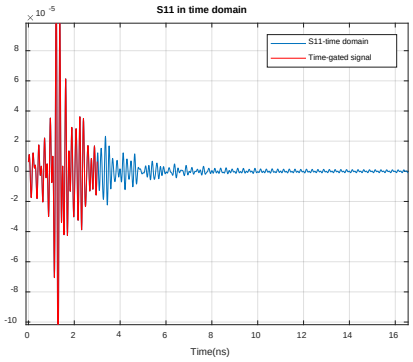

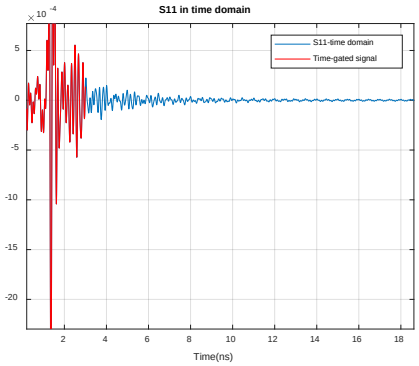

L=150 mm

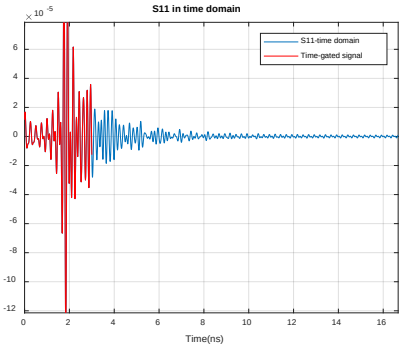

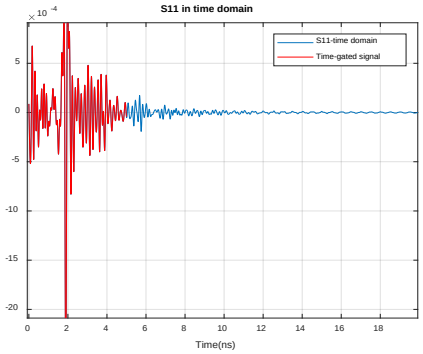

L=200 mm

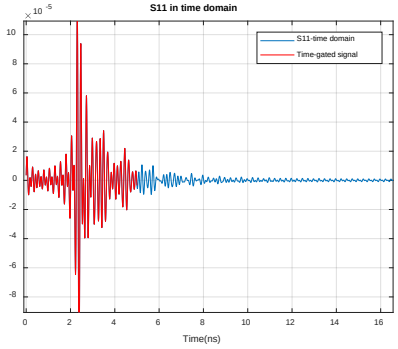

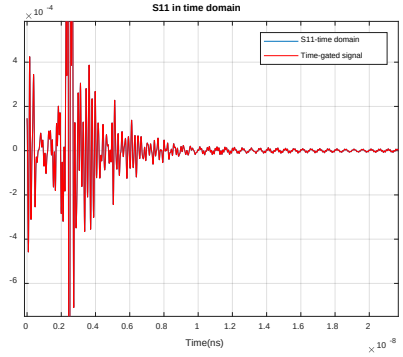

Figure 4-9 Validating simulated and measured signal peak from antenna-sensor with different transmission line lengths

In this chapter, the principle of wireless interrogation is explained. The design parameters for UWB and sensor part are also characterized. The measurement results shown in Figure 4-9 validate that the fabricated antennas with 100,150 and 200 mm length have time delays close to the simulation ones.

Chapter 5

Digital signal processing

5.1. Resolving signal interference issue by signal processing

Antenna resonant frequency will shift due to the applied pressure and shear forces. These changes in frequency can be determined from its reflection coefficient which is encoded in the reflected interrogation signal. The reflected interrogation signal radiates through the UWB antenna and received by the interrogator UWB antenna. As it is explained in the previous chapter, to generate proper delay time, we fabricated sensors with different transmission line lengths. Due to the round trip transmission on transmission line, the antenna backscattering corresponding to signal reflected by the antenna sensor has a specific time delay. Hence, it can be separated from the back-ground scattering in the time domain.

By applying Time Gating techniques on reflected signal received by the interrogator, the sensor mode data can be separated from back-ground scattering. Finally, the real-time resonant frequency of the antenna can be retrieved from its reflection coefficient.

5.2. Experimental setup

The experimental setup for validating the antenna sensor wireless interrogation is shown in Figure 5-1. The UWB and sensor are fabricated on RO3003 as it is discussed before. The sensor node package was placed inside an oven (Figure 5-2). The wireless interrogator was realized by using a VNA and two interrogation horn antennas.

Figure 5-1 Set up for wireless interrogation of antenna sensor

The horn antennas were placed at an interrogation distance of 70 cm in front of the UWB antenna. The S_{21} parameter between these two interrogation antennas was measured using VNA. The VNA was calibrated up to the feeding points of the interrogation antennas, which is 30 cm from the aperture of the interrogation antenna. Therefore, the wireless

transmission distance between the feeding points of the integration antennas and the antenna sensor is 100 cm.

Figure 5-2 Broadband Tx/Rx antenna connected to antenna sensor

5.3. Digital signal processing algorithm

We applied a DSP algorithm to the S_{21} parameter to extract the information from the backscattering. First, the S_{21} parameter acquired from the VNA, which has a frequency range from f_1 to f_2, is zero padded from the direct current (DC) frequency (i.e. 0 Hz) to f_1. The zero-padded S parameter is then converted to a time-domain signal using Inverse Fast Fourier Transform (IFFT). As shown in Figure 5-3, the resulting time-domain signal displays two major wave packets that correspond to the back-ground backscattering and the antenna sensor backscattering. Both wave packets have small side lobes, which can be reduced by windowing before the IFFT Nonetheless, the presents of the side lobes will not have an effect on

determining the frequency of the antenna sensor backscattering. Even though the signals backscattered by the Tx/Rx antenna and the surrounding structures usually have the largest amplitude, they appear at a different time span from that of the antenna sensor backscattering. Therefore, a gating window can be applied to the time domain signal to extract the antenna backscattering sensing signal [39].

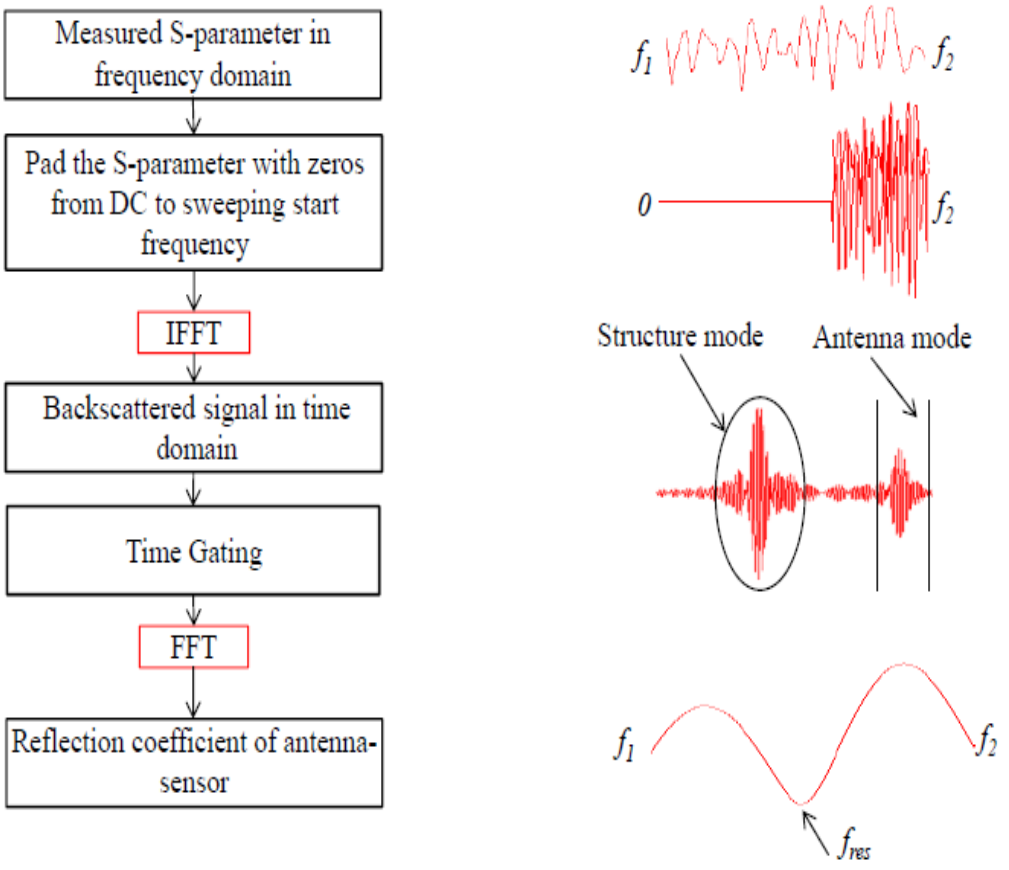

Figure 5-3 Flow diagram of digital signal processing algorithm and signal corresponds to processing blocks.

Since the time-gated signal will only contain signals that are reflected at or near the feeding point of the antenna sensor, the time gating process also eliminate reflections at other locations along the delay line. Subsequently, the gated signal is converted back to the frequency domain using Fast Fourier Transform (FFT) and the resonant frequency of the antenna-sensor can be determined as the frequency at which the reflection coefficient has the lowest value.

5.3. Results and discussion

By applying the proposed algorithm, the time-domain of a typical S_{21} parameter is shown in Figure 5-4.

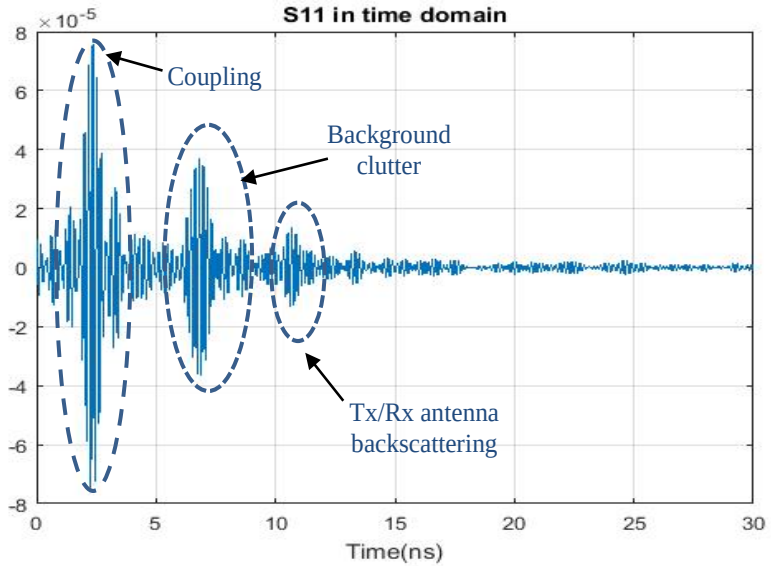

Figure 5-4 Time domain reflection signal converted from measured *S21* parameter

The first wave packet arrives at 2.6 ns which corresponding to round trip distance of 0.3 m, corresponding this distance between the feeding point of interrogation antenna and the antenna aperture. In other word, it results from the coupling between the two horn antennas. The second peak is the structural backscattering, which appears around 6.6 ns corresponds to the interrogation distance of 0.7 m. The last packets arrives 3.4 ns after the structure mode backscattering which is cause by the time delay introduced by microstrip delay line. By time gating the transmission signal between 10 to 13 ns, we can then separate the antenna mode backscattering. The resonant frequency of the antenna is determined by applying FFT of the time gated signal. The frequency spectra of the time gated signal is shown in Figure 5-5.

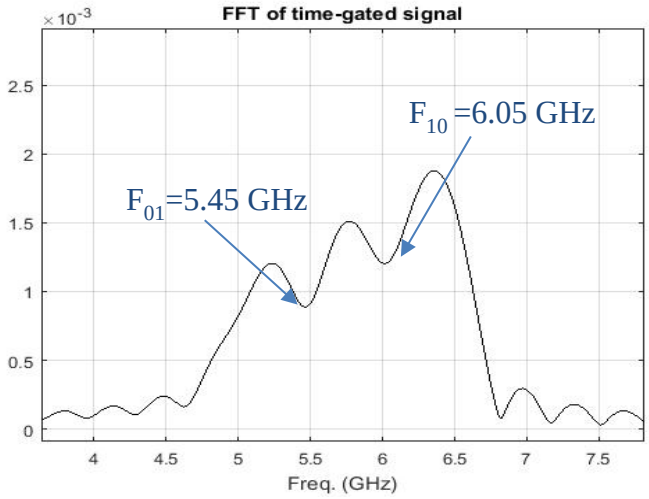

Figure 5-5 frequency spectrum of the gated time-domain signal

The resonant frequency of the antenna sensor is determined as the frequencies at which the frequency spectrum has the lowest amplitude.

5.4. Demonstrate wireless interrogation of the antenna sensor without any connectors:

After validating the performances of the antenna sensor and the Tx/Rx antenna separately using SMA connectors, both antennas were integrated on one RO3003 laminate by connecting them using a 200 mm microstrip transmission line. The entire sensor node was fabricated using chemical etching and the pictures of its front is shown in Figure 5-6.

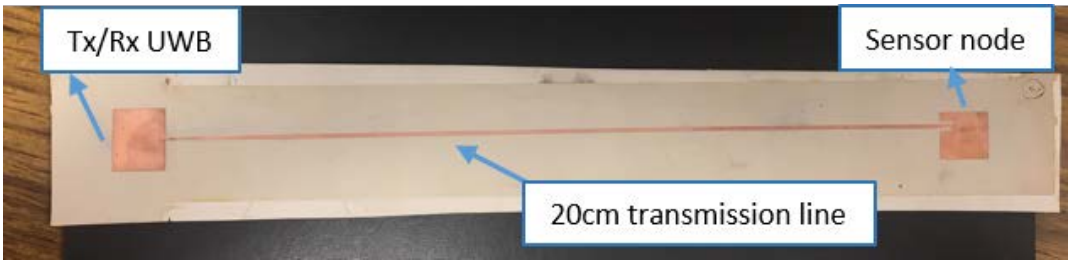

Figure 5-6 Tx/Rx antenna and antenna sensor fabricated on Rogers substrate

The experimental set up for wireless interrogation for the proposed sensor is shown in Figure 5-7. The sensor node was placed in the prosthetic socket covered by a liner. The wireless interrogator was realized by using a two circular UWB Tx/Rx antennas instead of two horn antennas. The UWB

Tx/Rx antenna was placed at an interrogation distance of 5 cm in front of Tx/Rx antenna. As a result, the wireless transmission distance between the interrogation antenna and the sensor node was 25 cm. Then, the S_{21} parameter between these two interrogation antennas was measured using the VNA, which was connected to the interrogation UWB Tx/Rx antenna using co-axial cable.

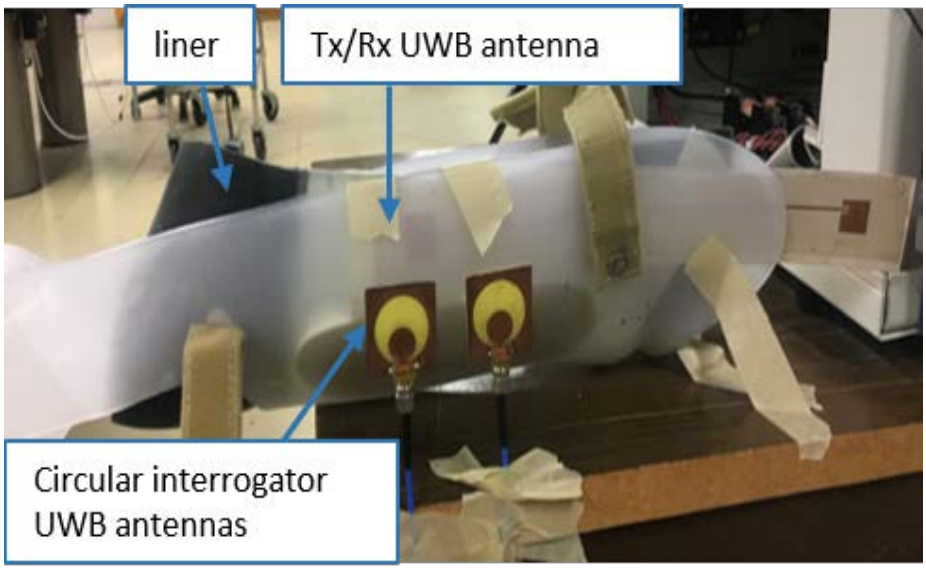

Figure 5-7 Tx/Rx antenna and antenna sensor placed in prosthetic socket for wireless interrogation

The measured S_{21} of the wireless interrogation set up was processed by the same DSP algorithm. The time domain signal is shown in Figure 5-8.

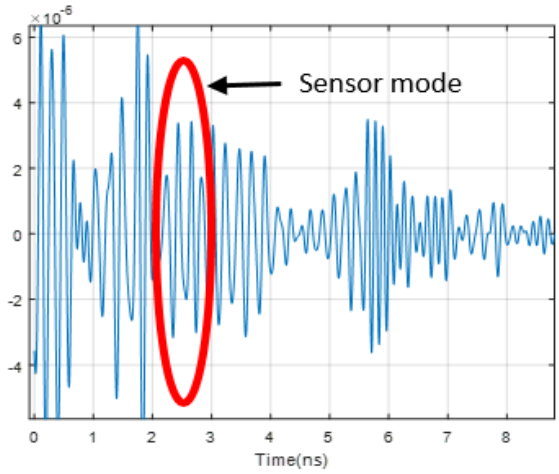

Figure 5-8 Time domain reflection signal converted from measured *S21* parameter

Finally, the antenna mode backscattering is extracted by time gating the transmission signal from 1.8 ns to 3 ns. The resonant frequency of the antenna sensor can then be determined by performing FFT of the time-gated signal. The extracted frequency spectrum is shown in Figure 5-9.

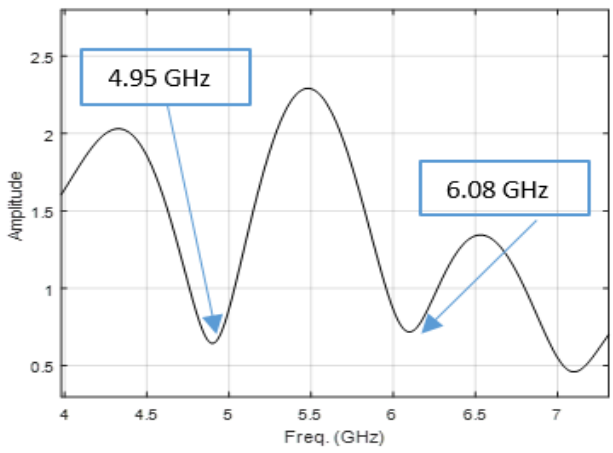

Figure 5-9 FFT of gated TD signal and extracted frequencies

Chapter 6

Wireless antenna sensor interrogation using FMCW –based interrogator

6.1. Operation principle

In the previous chapter, a wireless interrogation of the antenna sensor without any electronic components is demonstrated which is able to acquire the sensing signal in far field. This interrogator system has some limits; it is bulky, expensive and slow. Hence, in this chapter we are introducing a low-cost FMCW-based wireless interrogator. It decreases the cost and improves the interrogation speed because the time gating is performed in the frequency domain instead of the time domain.

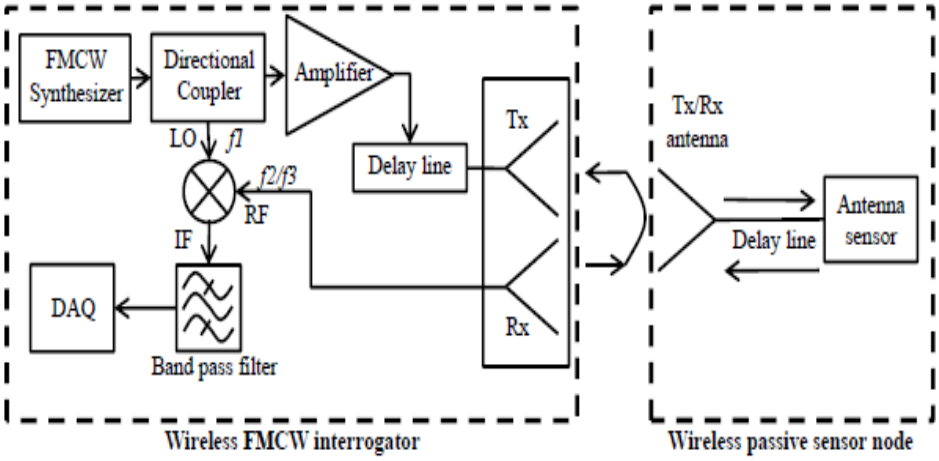

Figure 6-1 Proposed antenna-sensor wireless interrogation using FMCW time-gating technique

The same sensor package that we used in chapter 5 was still used but the VNA interrogator was replaced by the proposed FMCW interrogator. The block diagram for the system setup is depicted in Figure 6-1 [39]. A linear chirp signal with frequencies sweeping from f_1 to f_2 was generated and sent to the local port of the mixer and the directional coupler at the same time. As a result, both the frequency of the back-ground and the backscattering signals vary linearly with the time. Meanwhile, the Rx antenna receives a mixture of the back-ground scattering and sensor backscattering signal and send it to the RF port of the mixer. The mixer mixes the two input signals and produces an output frequency that is either the sum or difference of the input frequencies. The frequency of the back-ground scattering f_2 calculated based on time delay caused by delay line and the wireless transmission$d_{transmission}$:

$$f_2 = f_1 - \frac{W}{T}\left(d_{delay\ line} + d_{transmission}\right), \quad (4)$$

where *W* is the frequency sweeping range and *T* is the period of the FMCW signal. The third signal which is the backscattering sensing signal comes later due to the delay time introduced by the microstrip transmission line between sensor and UWB antennas. Its frequency, f_3, can be calculated as follows:

$$f_3 = f_1 - \frac{W}{T}\left(d_{delay\ line} + d_{transmission} + d_{transmission\ line}\right). \quad (5)$$

As a result, based on Equation 4 and Equation 5, there are two beat frequencies at the IF port of mixer *(f_2-f_1)* and *(f_3-f_1)* for the back-ground scattering and sensor signal, respectively. These two beat frequencies are separated due to the transmission line delay. In other words, it can be calculated as:

$$f_3 - f_2 = \frac{W.d_{transmission\ line}}{T}. \quad (6)$$

By using the proper band pass filter, we can then eliminate the back-ground clutter which is equivalent to performing time gating in the time domain. Performing time gating in the frequency domain, on the other hand, improved the interrogation speed of wireless receiver.

Since the power of the IF sensing signal is directly related to reflection coefficient S_{11} of the antenna sensor, the power of sensor signal is calculated as

$$P_s = P_t G_{tt} G_{tr} {G_r}^2 \frac{\lambda}{4\pi d} S_{11} L_d L_{mixer}, \quad (7)$$

here P_t is the transmit power of interrogation signal; $G_{tt}\ and\ G_{tr}$ are the radiation gains of the transmitter and receiver of the interrogator and G_r Is the radiation gain of UWB Tx/Rx antenna; λ is the wave length of

transmission electromagnetic (EM) wave; L_d is the loss caused by delay line and L_{mixer} is the down-conversion loss caused by RF mixer.

By collecting the filtered signal using a Data Acquisition (DAQ) system that has a 50 Ω input impedance, the real time amplitude will be:

$$A_s = \sqrt{50.P_s}\ . \tag{8}$$

Since, in each FMCW period, we will have the lowest reflection coefficient S_{11} when the interrogation frequencies match with sensor frequencies, as a result, the corresponds real-time amplitude A_s will be the smallest. Thus, by correlating the lowest amplitude of the collected signal in one FMCW period to the corresponding FMCW interrogation frequency, the resonant frequencies of the antenna can be determined[39]. Digital signal processing algorithm and corresponds signal are shown in Figure 6-2. In each FMCW period, the envelope of the input signal which is equal to the reflection coefficient of the antenna sensor was detected. The resonant frequencies of the antenna sensor then will be determined at the frequencies which has the lowest amplitude.

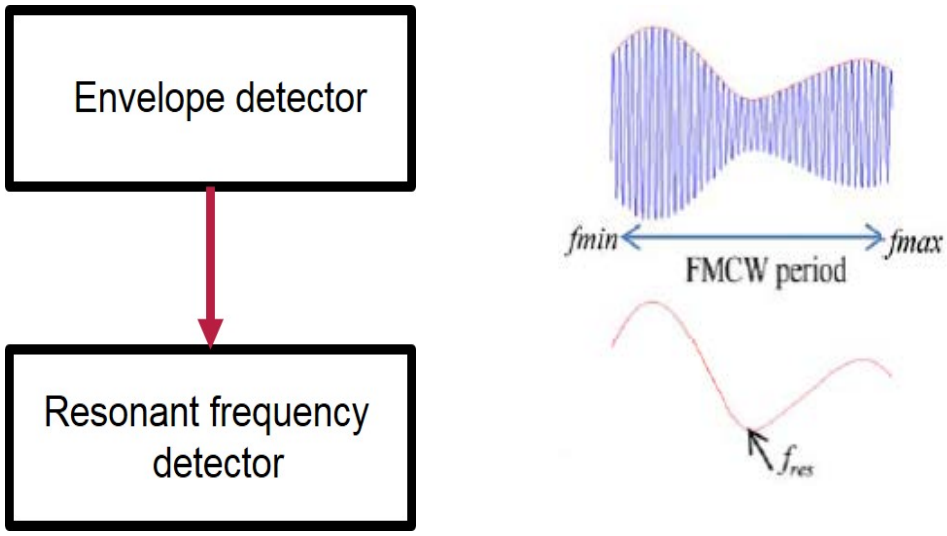

Figure 6-2 Digital signal processing algorithm and signal corresponding to each block

6.2. Characterizing the components for the FMCW interrogator circuit

Because the sensor that we introduced in chapter 4 has resonant frequencies at 5.35 and 6.05 GHz, we need to generate an interrogation signal with these frequencies range to excite the sensor. For this purpose, we used a Voltage control oscillator (VCO) controlled by a saw tooth signal. The saw tooth signal frequency was set as 1 kHz. The VCO we used is able to generate frequency between 1530 MHz up to 2700 MHz with a control voltage between 0.5 to 10 v. In order to have the frequency sweeping between 5 to 7 GHz, we used a frequency multiplier to triple the output frequency range of the VCO and thus increases the start and end frequency sweep to 4590 to 8100 MHz. Then, a BPF was used to limit the frequency

range from 4.9 to 6.9 GHz. The hardware setup for FMCW interrogator is shown in Figure 6-3. Due to the low output power for VCO (5 dBm), we need to increase the signal power by using a power amplifier.

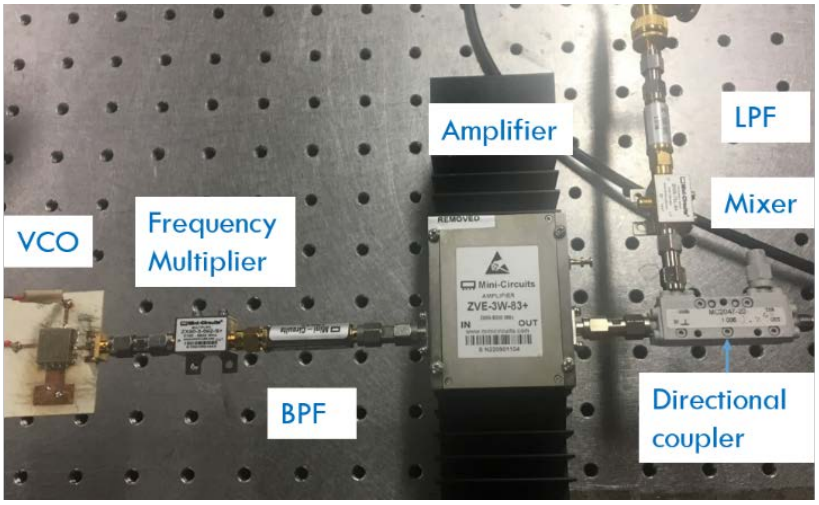

Figure 6-3 Implementation of FMCW interrogator

The amplified signal that is near to 25 dBm in power is sent to the directional coupler to direct a part of the signal to the Tx antenna through delay line and the other part is directed to the LO port of the mixer. The complete set up for FMCW interrogation is shown in Figure 6-4.

The interrogation distance between the Tx/Rx interrogator antennas was set as 0.5 m and the sensor with a 0.15 m transmission line is chosen.

By measuring the S_{11} parameter of the sensor with and without the delay line, the time delay caused by the delay line is determined. In other

words, we first collected the S_{11} parameter of the sensor without the delay line, then we added the delay line and again collect the S_{11} parameter. Both S_{11} parameters are then converted to the time domain signal using the DSP algorithm introduced in Figure 5-3.The converted time domain signal are presented in Figure 6-5 .

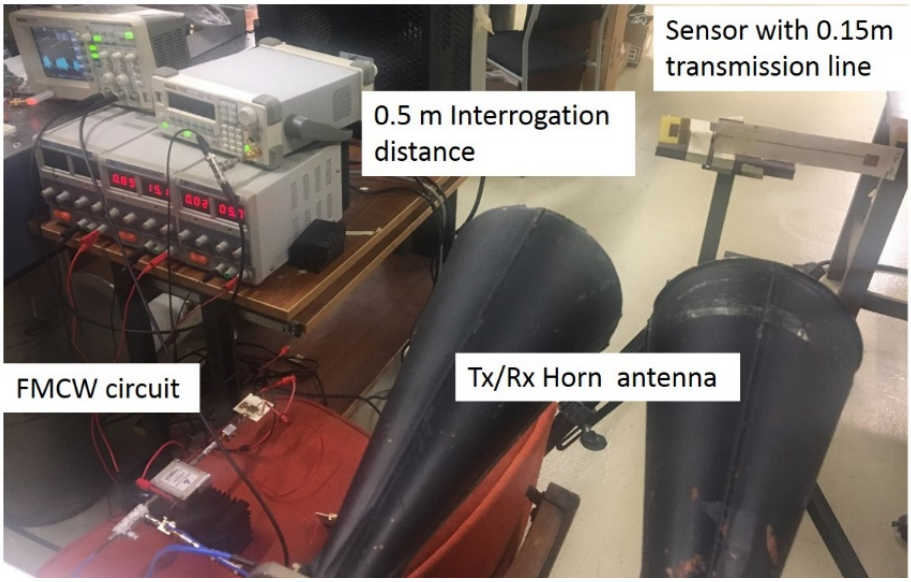

Figure 6-4 The complete set up for FMCW interrogation

Therefore, the total time delay can be measured based on the difference of these two peaks' arrival in time domain. Hence, based on the experimental result, the time delay caused by the delay line is considered as 29 ns.

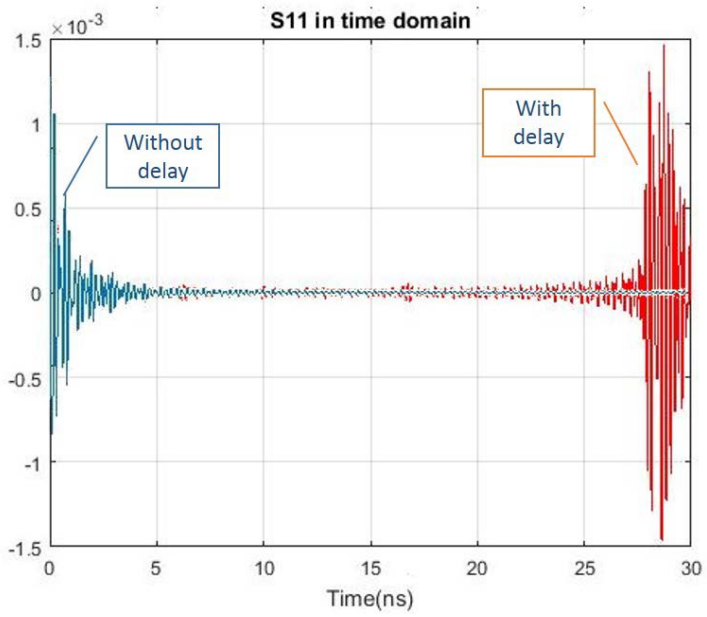

Figure 6-5 Time domain signals converted from S_{11}, without and with delay line

As it is shown in Figure 6-4, the signal travels to Tx antenna through the delay line and gets to the sensor. Then the reflected signal from sensor is received by Rx antenna and goes to the RF port of the mixer. The IF port of the mixer contains two frequency component as we explained before: back-ground scattering and sensor node signal. The frequency of signal at IF port of the mixer is determined as:

$$IF = \frac{W * total\ delay}{T} \quad , \qquad (9)$$

here W is the frequency sweeping range between 4.9 and 6.2 GHz and T is FMCW interrogation period which equals to 1 ms.

Then, to eliminate the high frequency noise, a low pass filter is used. The filtered signal is then collected by an oscilloscope for signal processing procedure.

6.3. Digital signal processing algorithm

BY collecting the S_{21} parameter from the oscilloscope, a DSP algorithm was used in MATLAB to process the data. The goal is to separate the sensor backscattering signal and back-ground scattering and then extracting the resonant frequency of the sensor from the frequency spectrum. The steps are illustrated in Figure 6-6.

First of all, the S_{21} collected-data divided into arrays for each FMCW period. As it is shown in Figure 6-6, the frequency spectrum includes many frequency components including the coupling between the interrogation antennas, back-ground clutter and sensor node signal[39].

In order to separate the sensor signal, we used the BPF. By converting the filtered signal into frequency domain, based on Equation 8, we conclude that, the amplitude of this signal is proportional to the reflection coefficient of the antenna sensor. Next, by applying envelope detection algorithm we track the amplitude in FMCW sweeping frequency range. As it was explained before, the lowest amplitude in the envelope curve corresponds to the antenna sensor resonant frequencies.

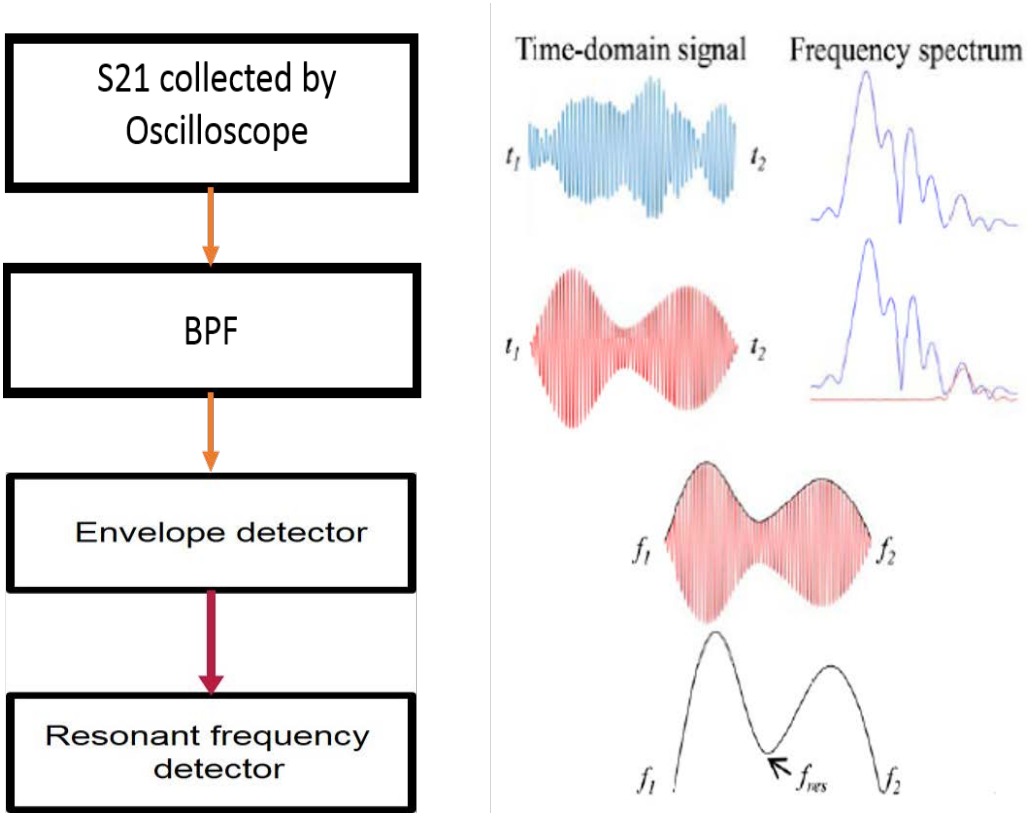

Figure 6-6 Flow diagram and related signals for MATLAB DSP algorithm

6.4. Results and discussion

Based on the set up in Figure 6-4, the S_{21} parameter was collected from the oscilloscope. The interrogation distance was set as 0.50 m. By applying the DSP algorithm explained in previous part, the resonant frequencies of the antenna are extracted as shown in Figure 6-7.

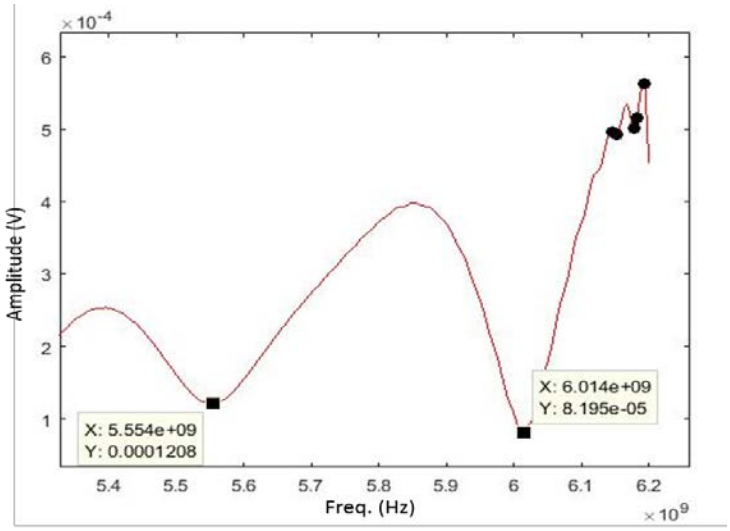

Figure 6-7 Measured antenna-sensor's reflection coefficients at different temperatures using FMCW interrogator

The resonant frequencies extracted using the FMCW interrogator match the results from the VNA based interrogator.

In this chapter an FMCW-based wireless interrogator for the antenna sensor was introduced. Instead of performing time gating in the time domain, we performed the time gating in the frequency domain. This method can be used to acquire data from the shear and pressure sensor, which is located in medical devices such as prosthetic socket or walkers, to the DAQ device to measure the displacement based on the changes in frequencies. It can be used for real time fitting of assistive medical devices.

Chapter 7

Conclusion and future work

In this study, we first investigated a dual-frequency stacked microstrip patch antenna sensor for simultaneous shear and pressure displacement measurements. By constructing the dual-frequency antenna sensor using a rectangular microstrip patch antenna, a superstrate, and a director, we demonstrated that the shear and pressure displacements between the radiation patch and the director can be inversely determined from the measured antenna resonant frequencies. The typical measurement errors were found to be ±0.3mm for the shear displacement and within ±0.15 mm for the pressure displacement. Multiplexing the antenna sensors to form distributed sensor arrays will be investigated in the future.

The wireless interrogation of passive antenna sensor based on antenna backscattering is also investigated. The UWB Tx/Rx antenna as a passive transceiver, was then fabricated on the flexible substrate. In order to distinguish the sensor backscattering from the background scattering, a microstrip transmission line was added to connect the Tx/Rx antenna and microstrip patch antenna in sensor node side. The transmission line delays the signal reflected from the sensing element and separated it from

background scattering. By applying a DSP algorithm, the back-ground scattering was separated from sensor backscattering and the resonant frequencies were extracted.

Finally, a Frequency Modulated Continue Wave (FMCW) generator was developed to detect antenna resonant frequencies. The battery-powered portable interrogator was developed to facilitate real-time monitoring on a continuous basis. As a result, the interrogation speed of wireless interrogation is improved. By implementing a compact PCB FMCW synthesizer the circuit size was also minimized.

In future, this wireless interrogation system can be used to send and receive data to network of sensors. Due to the specific time delay caused by the delay line sensing information of each sensor can be separated from others. The proposed shear/pressure displacement sensor is intended to be used for monitoring the interaction between the human body and assistive medical devices such as prosthetic liner and diabetic shoes.

References

[1] M. T. Francomano, D. Accoto, and E. Guglielmelli, “Artificial Sense of Slip—A Review,” *IEEE Sens. J.*, vol. 13, no. 7, pp. 2489–2498, 2013.

[2] S. K. Hwang and H. Y. Hwang, “Study on signal characteristic analysis of multi-axis load measurement sensors,” *Smart Mater. Struct.*, vol. 25, no. 11, 2016.

[3] C. Guo, L. Zhou, and J. Lv, “Effects of expandable graphite and modified ammonium polyphosphate on the flame-retardant and mechanical properties of wood flour-polypropylene composites,” *Polym. Polym. Compos.*, vol. 21, no. 7, pp. 449–456, 2013.

[4] M. Y. Cheng, C. L. Lin, Y. T. Lai, and Y. J. Yang, “A polymer-based capacitive sensing array for normal and shear force measurement,” *Sensors (Switzerland)*, vol. 10, no. 11, pp. 10211–10225, 2010.

[5] J. Missinne *et al.*, “Two axis optoelectronic tactile shear stress sensor,” *Sensors Actuators, A Phys.*, vol. 186, pp. 63–68, 2012.

[6] S. Rajala and J. Lekkala, “Plantar shear stress measurements - A review,” *Clin. Biomech.*, vol. 29, no. 5, pp. 475–483, 2014.

[7] M. Yavuz, H. Master, A. Garrett, L. A. Lavery, and L. S. Adams, “Peak plantar shear and pressure and foot ulcer locations: A call to revisit ulceration pathomechanics,” *Diabetes Care*, vol. 38, no. 11, pp. e184–e185, 2015.

[8] J. S. Akins, P. E. Karg, and D. M. Brienza, “Interface shear and pressure characteristics of wheelchair seat cushions,” *J. Rehabil. Res. Dev.*, vol. 48, no. 3, p. 225, 2011.

[9] a F. Mak, M. Zhang, and D. a Boone, “State-of-the-art research in lower-limb prosthetic biomechanics-socket interface: a review.,” *J. Rehabil. Res. Dev.*, vol. 38,

no. 2, pp. 161–174, 2001.

[10] F. A. Appoldt, L. Bennett, and R. Contini, “Tangential Pressure Measurement in Above-Knee Suction Sockets,” *Bull. Prosthet. Res.*, no. 13, pp. 70–86, 1970.

[11] D. Benfield, E. Lou, and W. A. Moussa, “Parametric evaluation of shear sensitivity in piezoresistive interfacial force sensors,” *J. Micromechanics Microengineering*, vol. 21, no. 4, 2011.

[12] Y. Jung, D. G. Lee, J. Park, H. Ko, and H. Lim, “Piezoresistive tactile sensor discriminating multidirectional forces,” *Sensors (Switzerland)*, vol. 15, no. 10, pp. 25463–25473, 2015.

[13] M. C. Hsieh *et al.*, “A contact-type piezoresistive micro-shear stress sensor for above-knee prosthesis application,” *J. Microelectromechanical Syst.*, vol. 10, no. 1, pp. 121–127, 2001.

[14] P. Laszczak *et al.*, “A pressure and shear sensor system for stress measurement at lower limb residuum/socket interface,” *Med. Eng. Phys.*, vol. 38, no. 7, pp. 695–700, 2016.

[15] C. Murakami, Y. Ishikuro, and M. Takahashi, “Feasibility of novel four degrees of freedom capacitive force sensor for skin interface force,” *Biomed. Eng. Online*, vol. 11, no. 1, p. 90, 2012.

[16] K. Sundara-Rajan, G. I. Rowe, A. Bestick, A. V. Mamishev, G. K. Klute, and W. R. Ledoux, “Capacitive sensing of interfacial forces in prosthesis,” *2010 IEEE Int. Work. Med. Meas. Appl. MeMeA 2010 - Proc.*, no. 2, pp. 73–76, 2010.

[17] L. Du, X. Zhu, and J. Zhe, “An inductive sensor for real-time measurement of plantar normal and shear forces distribution,” *IEEE Trans. Biomed. Eng.*, vol. 62, no. 5, pp. 1316–1323, 2015.

[18] Z. F. Zhang, X. M. Tao, H. P. Zhang, and B. Zhu, “Soft fiber optic sensors for

precision measurement of shear stress and pressure," *IEEE Sens. J.*, vol. 13, no. 5, pp. 1478–1482, 2013.

[19] W.-C. Wang, W. R. Ledoux, B. J. Sangeorzan, and P. G. Reinhall, "A shear and plantar pressure sensor based on fiber-optic bend loss," *J. Rehabil. Res. Dev.*, vol. 42, no. 3, p. 315, 2005.

[20] A. Candiani, W. Margulis, M. Konstantaki, and S. Pissadakis, "Ferrofluid-infiltrated optical fibers for shear-sensing smart pads," *SPIE Newsroom*, pp. 11–13, 2012.

[21] G. Marrocco, L. Mattioni, and C. Calabrese, "Multiport sensor RFIDs for wireless passive sensing of objects - Basic theory and early results," *IEEE Trans. Antennas Propag.*, vol. 56, no. 8 II, pp. 2691–2702, 2008.

[22] S. Caizzone and G. Marrocco, "RFID-grids for deformation sensing," *2012 IEEE Int. Conf. RFID, RFID 2012*, pp. 130–134, 2012.

[23] C. Mandel, B. Kubina, M. Schüßler, and R. Jakoby, "Passive Chipless Wireless Sensor for Two-Dimensional Displacement Measurement," *41st Eur. Microw. Conf.*, no. October, pp. 79–82, 2011.

[24] D. J. Thomson, D. Card, and G. E. Bridges, "RF Cavity Passive Wireless Sensors With Time-Domain Gating-Based Interrogation for SHM of Civil Structures," *IEEE Sens. J.*, vol. 9, no. 11, pp. 1430–1438, 2009.

[25] T. T. Thai, H. Aubert, P. Pons, G. Dejean, M. Mtentzeris, and R. Plana, "Novel design of a highly sensitive RF strain transducer for passive and remote sensing in two dimensions," *IEEE Trans. Microw. Theory Tech.*, vol. 61, no. 3, pp. 1385–1396, 2013.

[26] H. Aubert *et al.*, "Wireless sensing and identification based on radar cross section variability measurement of passive electromagnetic sensors," *Ann. des Telecommun. Telecommun.*, vol. 68, no. 7–8, pp. 425–435, 2013.

[27] H. Huang, “Antenna Sensors in Passive Wireless Sensing Systems,” *Handb. Antenna Technol.*, pp. 1–34, 2015.

[28] H. Huang, “Flexible wireless antenna sensor: A review,” *IEEE Sens. J.*, vol. 13, no. 10, pp. 3865–3872, 2013.

[29] A. Daliri, A. Galehdar, W. S. Rowe, K. Ghorbani, and S. John, “Utilising microstrip patch antenna strain sensors for structural health monitoring,” *J. Intell. Mater. Syst. Struct.*, vol. 23, no. 2, pp. 169–182, 2012.

[30] Z. Lei and W. Zhi, “Integration of RFID into wireless sensor networks: Architectures, opportunities and challenging problems,” *Proc. - Fifth Int. Conf. Grid Coop. Comput. GCC 2006 - Work.*, pp. 463–469, 2006.

[31] “31-Antenna_Theory_Analysis_and_Design(3rd_Edition)_pdf - Google Drive.” .

[32] I. Bahl, P. Bhartia, and S. Stuchly, “Design of microstrip antennas covered with a dielectric layer,” *IEEE Trans. Antennas Propag.*, vol. 30, no. 2, pp. 314–318, 1982.

[33] “33-.” .

[34] B. Kaur, G. Saini, and A. Saini, “Silicone Rubber Superstrate Loaded Patch Antenna Design Using Slotting Technique,” *IOP Conf. Ser. Mater. Sci. Eng.*, vol. 149, no. 1, pp. 0–8, 2016.

[35] U. Tata, H. Huang, R. L. Carter, and J. C. Chiao, “Exploiting a patch antenna for strain measurements,” *Meas. Sci. Technol.*, vol. 20, no. 1, 2009.

[36] A. H. Abdul Razak, A. Zayegh, R. K. Begg, and Y. Wahab, “Foot plantar pressure measurement system: A review,” *Sensors (Switzerland)*, vol. 12, no. 7, pp. 9884–9912, 2012.

[37] G. Breed, “A summary of FCC rules for ultra wideband communications,” *High Freq. Electron.*, vol. 4, no. 1, pp. 42–44, 2005.

[38] C. E. Balanis, “Antenna Theory: Analysis and Design, 3rd Edition - Constantine A.

Balanis," *Book*. p. 1136, 2005.

[39] J. Yao, F. Mbanya Tchafa, A. Jain, S. Tjuatja, and H. Huang, "Far-Field Interrogation of Microstrip Patch Antenna for Temperature Sensing Without Electronics," *IEEE Sens. J.*, vol. 16, no. 19, pp. 7053–7060, 2016.